UNITED STATES
DEPARTMENT OF
COMMERCE
PUBLICATION

NOAA Technical Report NESS 55

U.S. DEPARTMENT OF COMMERCE
National Oceanic and Atmospheric Administration
National Environmental Satellite Service

The Use of Satellite-Observed Cloud Patterns in Northern-Hemisphere 500-mb Numerical Analysis

ROLAND E. NAGLE AND CHRISTOPHER M. HAYDEN

WASHINGTON, D.C.
April 1971

National Environmental Satellite Service Series

The National Environmental Satellite Service (NESS) is responsible for the establishment and operation of the National Operational Meteorological Satellite System and of the environmental satellite systems of NOAA. The three principal Offices of NESS are Operations, Systems Engineering, and Research. The NOAA Technical Report NESS series is used by these Offices to facilitate early distribution of research results, data handling procedures, systems analyses, and other information of interest to NOAA organizations.

Publication of a Report in NOAA Technical Report NESS series will not preclude later publication in an expanded or modified form in scientific journals. NESS series of NOAA Technical Reports is a continuation of, and retains the consecutive numbering sequence of, the former series, ESSA Technical Report National Environmental Satellite Center (NESC), and of the earlier series, Weather Bureau Meteorological Satellite Laboratory (MSL) Report. Reports 1 to 37 are listed in publication NESC 56 of this series.

Reports 1 to 50 in the series are available from the National Technical Information Service, U.S. Department of Commerce, Sills Bldg., 5285 Port Royal Road, Springfield, Va. 22151. Price: $3.00 paper copy; $0.95 microfiche. Order by accession number, when given, at end of each entry. Beginning with 51, Reports are available through the Superintendent of Documents, U.S. Government Printing Office, Washington, D.C. 20402.

ESSA Technical Reports

NESC 38. Angular Distribution of Solar Radiation Reflected from Clouds as Determined from TIROS IV Radiometer Measurements, I. Ruff, R. Koffler, S. Fritz, J. S. Winston, and P. K. Rao, March 1967. (PB 174 729)

NESC 39. Motions in the Upper Troposphere as Revealed by Satellite Observed Cirrus Formation, H. McClure Johnson, October 1966. (PB 173 996)

NESC 40. Cloud Measurements Using Aircraft Time-Lapse Photography, L. F. Whitney, Jr., and E. Paul McClain, April 1967. (PB 174 728)

NESC 41. The SINAP Problem: Present Status and Future Prospects. Proceedings of a Conference held at the National Environmental Satellite Center, Suitland, Md., January 18-20, 1967, E. Paul McClain, Reporter, October 1967. (PB 176 570)

NESC 42. Operational Processing of Low Resolution Infrared (LRIR) Data from ESSA Satellites, Louis Rubin, February 1968. (PB 178 123)

NESC 43. Atlas of World Maps of Long-Wave Radiation and Albedo -- For Seasons and Months Based on Measurements from TIROS IV and TIROS VII, J. S. Winston and V. Ray Taylor, September 1967. (PB 176 569)

NESC 44. Processing and Display Experiments Using Digitized ATS-1 Spin Scan Camera Data, M. B. Whitney, R. C. Doolittle, and B. Goddard, April 1968. (PB 178 424)

NESC 45. The Nature of Intermediate-Scale Cloud Spirals, Linwood F. Whitney, Jr., and Leroy D. Herman, May 1968. (AD-673 681)

NESC 46. Monthly and Seasonal Mean Global Charts of Brightness From ESSA 3 and ESSA 5 Digitized Pictures, February 1967-February 1968, V. Ray Taylor and Jay S. Winston, November 1968. (PB 180 717)

NESC 47. A Polynomial Representation of Carbon Dioxide and Water Vapor Transmission, William L. Smith, February 1969. (PB-183 296)

NESC 48. Statistical Estimation of the Atmosphere's Geopotential Height Distribution From Satellite Radiation Measurements, William L. Smith, February 1969. (PB 183 297)

NESC 49. Synoptic/Dynamic Diagnosis of a Developing Low-Level Cyclone and Its Satellite-Viewed Cloud Patterns, Harold J. Brodrick and E. Paul McClain, May 1969. (PB 184 612)

NESC 50. Estimating Maximum Wind Speed of Tropical Storms from High Resolution Infrared Data, L. F. Hubert, A. Timchalk, and S. Fritz, May 1969. (PB 184 611)

NESC 51. Application of Meteorological Satellite Data in Analysis and Forecasting, R. K. Anderson, J. P. Ashman, F. Bittner, G. R. Farr, E. W. Ferguson, V. J. Oliver, and A. H. Smith, September 1969. (AD-697 033)

NESC 52. Data Reduction Processes for Spinning Flat-Plate Satellite-Borne Radiometers, Torrence H. MacDonald, July 1970.

NESC 53. Archiving and Climatological Applications of Meteorological Satellite Data, John A. Leese, Arthur L. Booth, and Frederick A. Godshall, July 1970. (COM-71-00076)

NESC 54. Estimating Cloud Amount and Height From Satellite Infrared Radiation Data, P. Krishna Rao, July 1970. (PB-194 685)

NESC 56. Time Longitude Sections of Tropical Cloudiness (December 1966-November 1967), J. M. Wallace, July 1970.

NOAA Technical Reports

NESS 57. The Use of Satellite-Observed Cloud Patterns in Northern Hemisphere 500-mb Numerical Analysis, Roland E. Nagle and Christopher M. Hayden, April 1971.

U.S. DEPARTMENT OF COMMERCE
Maurice H. Stans, Secretary
NATIONAL OCEANIC AND ATMOSPHERIC ADMINISTRATION
Robert M. White, Administrator
NATIONAL ENVIRONMENTAL SATELLITE SERVICE
David S. Johnson, Director

NOAA Technical Report NESS 55

The Use of Satellite-Observed Cloud Patterns in Northern Hemisphere 500-mb Numerical Analysis

ROLAND E. NAGLE AND CHRISTOPHER M. HAYDEN

WASHINGTON, D.C.
APRIL 1971

UDC 551.509.314:551.547.5:551.507.362.2:551.576.1

551.5	Meteorology
.507.362.2	Weather Satellites
.509.314	Objective forecasting techniques
.547.5	Constant pressure levels
.576.1	Cloud patterns

For sale by the Superintendent of Documents, U.S. Government Printing Office
Washington, D.C. 20402 - Price 55 cents

CONTENTS

THE USE OF SATELLITE-OBSERVED CLOUD PATTERNS IN NORTHERN HEMISPHERE 500-MB NUMERICAL ANALYSIS

Roland E. Nagle and Christopher M. Hayden

ABSTRACT. A quasi-objective method for deriving 500-mb geopotential heights with the aid of satellite cloud observations is presented. The method uses satellite-observed cloud patterns in conjunction with a forecast 500-mb height field which is separated into additive short- and long-wave component fields. Empirical relationships between the cloud patterns and the short-wave component field are used to modify the pattern of the latter, and regression equations are used to specify extrema values. The 500-mb heights are retrieved by the direct addition of the modified short-wavelength field to the long-wavelength field. Procedures for using this method operationally are presented, and results of real-time application are shown. It is concluded that the resulting modifications can contribute to significant improvements in the analysis.

1. INTRODUCTION

Prerequisite to the use of satellite cloud data in numerical weather analysis is the establishment of consistent relationships between cloud patterns and parameters which can be used in or readily transformed into data suitable for a numerical analysis system. The literature is abundant with reports on the relationships between cloud pattern features and descriptive features of synoptic meteorology, i.e., fronts, troughs, ridges, jet streams, etc. The results of these studies, which were first consolidated by Widger (1964), provide a useful background for interpreting satellite-observed cloud patterns, but do not offer a means for utilizing these data in numerical weather analysis.

An approach to this problem was first proposed by Bristor and Ruzecki (1960). They suggest that use be made of the approximate relationship between clouds and vertical motion at 500-mb as expressed in the vorticity advection term of the quasi-geostrophic "Omega Equation." The procedure required the modification of the height or the stream function field (or their Laplacians) at the 500-mb level on the basis of satellite-observed cloud patterns. McClain, Brodrick, and Ruzecki (1965, 1966) attempted reanalyses using these relationships, and Bradley, Hayden, and Wiin-Nielsen (1966) used this approach in further experiments.

The approach as reported by these investigators has certain limitations. Although modifying the Laplacian field changes the vorticity advection, the effects are not known until after the height field or stream function field is retrieved by relaxation. Relaxation also obstructs preservation of conventional data and, if total vorticity is not conserved within the reanalysis area, can cause changes outside the reanalysis area when the height or stream function field is retrieved. The magnitude of modifications in the Laplacian field is critical and cannot be established objectively. Finally, care must be taken in the reanalysis to insure that negative absolute vorticities are not produced.

The approach presented in this report is an extension of Bristor's and Ruzecki's (1960) suggestions with several significant variations. Also, it is a simplification of a system first proposed by Nagle, et. al., (1966) and developed by Nagle and Clark (1968). The approach is analogous to perturbation theory in that it requires the objective separation of the 500-mb height field into additive long- and short-wavelength components, i. e., the spatial mean flow and superimposed disturbances. The good relationship found between the cloud patterns and certain features of the short-wavelength field permits manual modification of the latter in areas of sparse conventional data. The use of relaxation techniques to retrieve the 500-mb height values is not required because the direct addition of the short- and long-wavelength components produces the modified 500-mb height field. Statistical methods are used to derive regression equations from which the magnitude of extrema in the short-wavelength field can be computed objectively. The modifications effected in the total height field are relatively minor and do not significantly change the pattern of the long-wavelength field. Thus, the vorticity advection at 500 mb is also adjusted to conform to the observed cloud patterns (Nagle and Clark, 1968). The results indicate that, with proper interpretation of the cloud patterns, the short-wavelength features of the 500-mb height field can be correctly introduced into numerical analysis.

2. SEPARATION BY SCALE

The method for objectively separating meteorological fields into additive components was developed by Holl (1963). The technique, essentially an objective version of Fjortoft's (1952) method, successively applies a smoothing operator to a numerical field until the amplitude of a specified wavelength component is reduced to a specified percentage of its initial value. Since the operator is linear, all additions and subtractions to yield components of the initial field are commutative.

The smoothing is defined by (Holl, 1963):

$$Z_{LW} = Z_0 + C\int_0^{\alpha} \nabla^2 Z \, d\alpha = Z_0 - Z_{SW} \tag{1}$$

where Z_{LW} is the long-wavelength field, Z_0 is the original field, Z_{SW} is the short-wavelength field, C is a constant, and α is a parameter representing the degree of smoothing. Appendix B contains a detailed discussion of the smoothing procedure; Appendix C is the computer program which performs the smoothing.

The degree of smoothing to be applied is somewhat arbitrary, but there is evidence[1] that a reasonable separation can be made between the short- and long-wave components at 500 mb with the degree of smoothing set at $\alpha = 5$. For this amount of smoothing the amplitude of a system with a wavelength of 7 gridlengths (1 gridlength = 381 km at 60° N.) is reduced to 5 percent of its initial value. A system of this size corresponds approximately to zonal wave number 10 at 45° N. In contrast, the amplitude of a system with wave number 3 (23 gridlengths) is reduced by less than 4 percent. The degree of smoothing used throughout this study was $\alpha = 5$. The corresponding amplitude reduction as a function of wavelength (in gridlengths) is shown in figure 1.

Figures 2 through 4 are examples of the fields produced by the scale separation technique. Figure 2 is an initial 500 mb height field; figure 3 is the field produced by the smoothing process, i. e., the long-wave pattern. By subtracting the long-wave field from the initial 500-mb analysis at gridpoints, the components which have been smoothed out of the initial analysis can be retrieved. The short-wavelength component field corresponding to figures 2 and 3 is shown in figure 4.

3. SIGNIFICANCE OF THE SHORT-WAVELENGTH COMPONENT

The short-wavelength component field is significant because it approximates the field of relative vorticity. Certain characteristic features of the cloud patterns are related to the 500-mb relative vorticity field and therefore to the short-wavelength field (see, for example, Nagle, et. al., 1966). Thus, configurations of the satellite-observed cloud field may be used to modify the short-wavelength component field. These short-wave modifications are in turn easily incorporated in the total height field by simple addition to the long-wavelength component field. We shall first discuss the relationship between the short-wave and relative vorticity fields and then describe relationships between the relative vorticity and the cloud patterns.

From (1) the short-wavelength component is given by

$$Z_{SW} \mp -C\int_0^{\alpha} \nabla^2 Z \, d\alpha \tag{2}$$

[1]Meteorology International Inc., Quarterly Performance Report No. 4, Contract No. N00228-67-C-2759, Monterey, Calif., September, 1968.

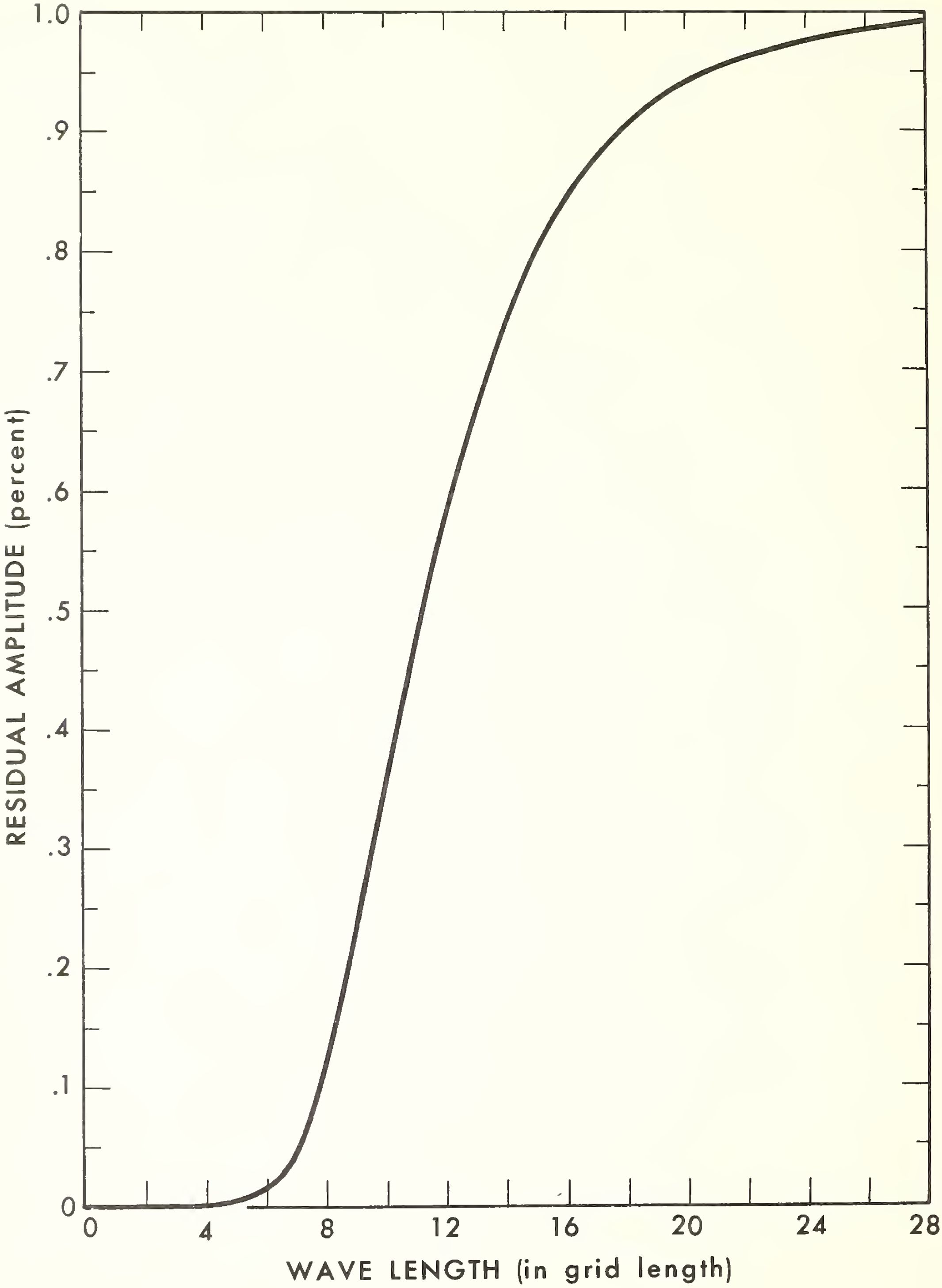

Figure 1.--Filter curve for smoothing (α = 5). One gridlength equals 361 km at 60° N.

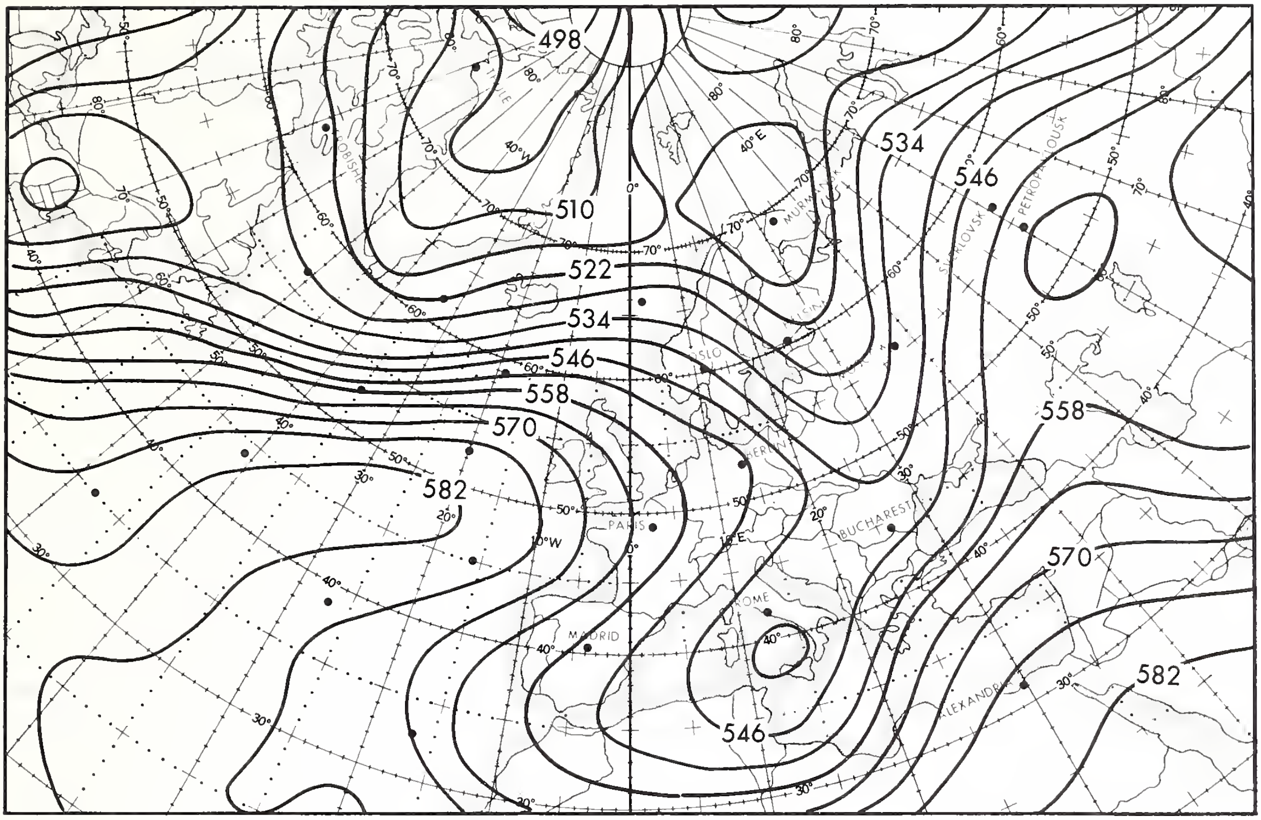

Figure 2.--500-mb geopotential height field (decameters), 1200 GMT, March 16, 1970.

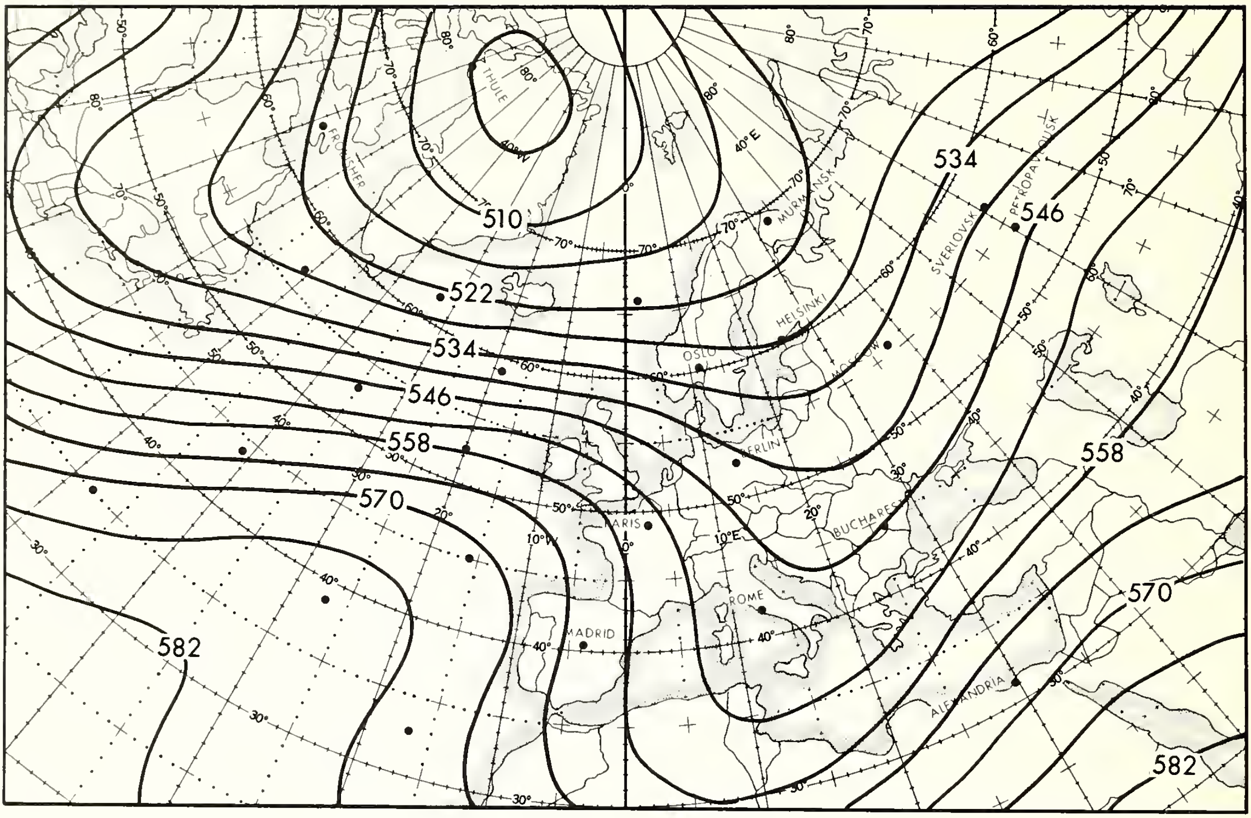

Figure 3.--500-mb long-wavelength field (decameters), 1200 GMT, March 16, 1970.

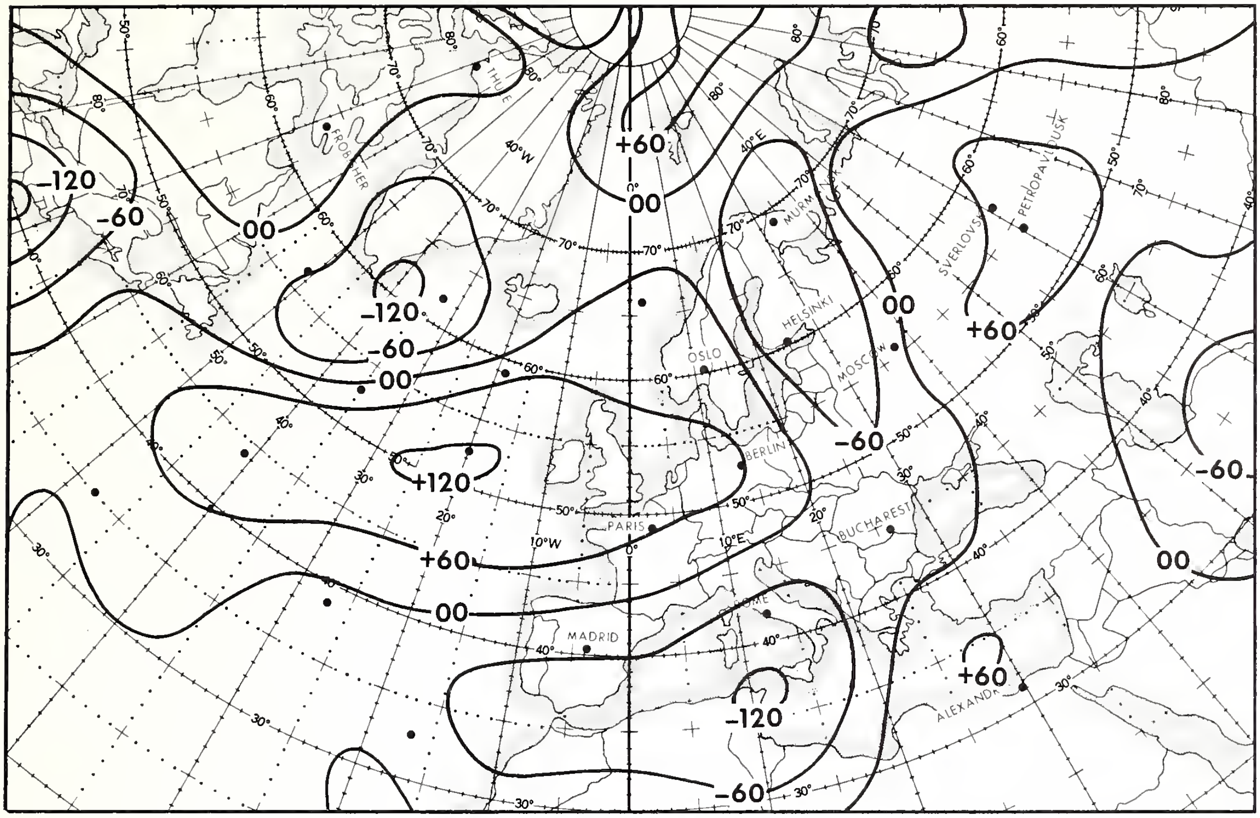

Figure 4.--500-mb short-wavelength field (meters), 1200 GMT, March 16, 1970.

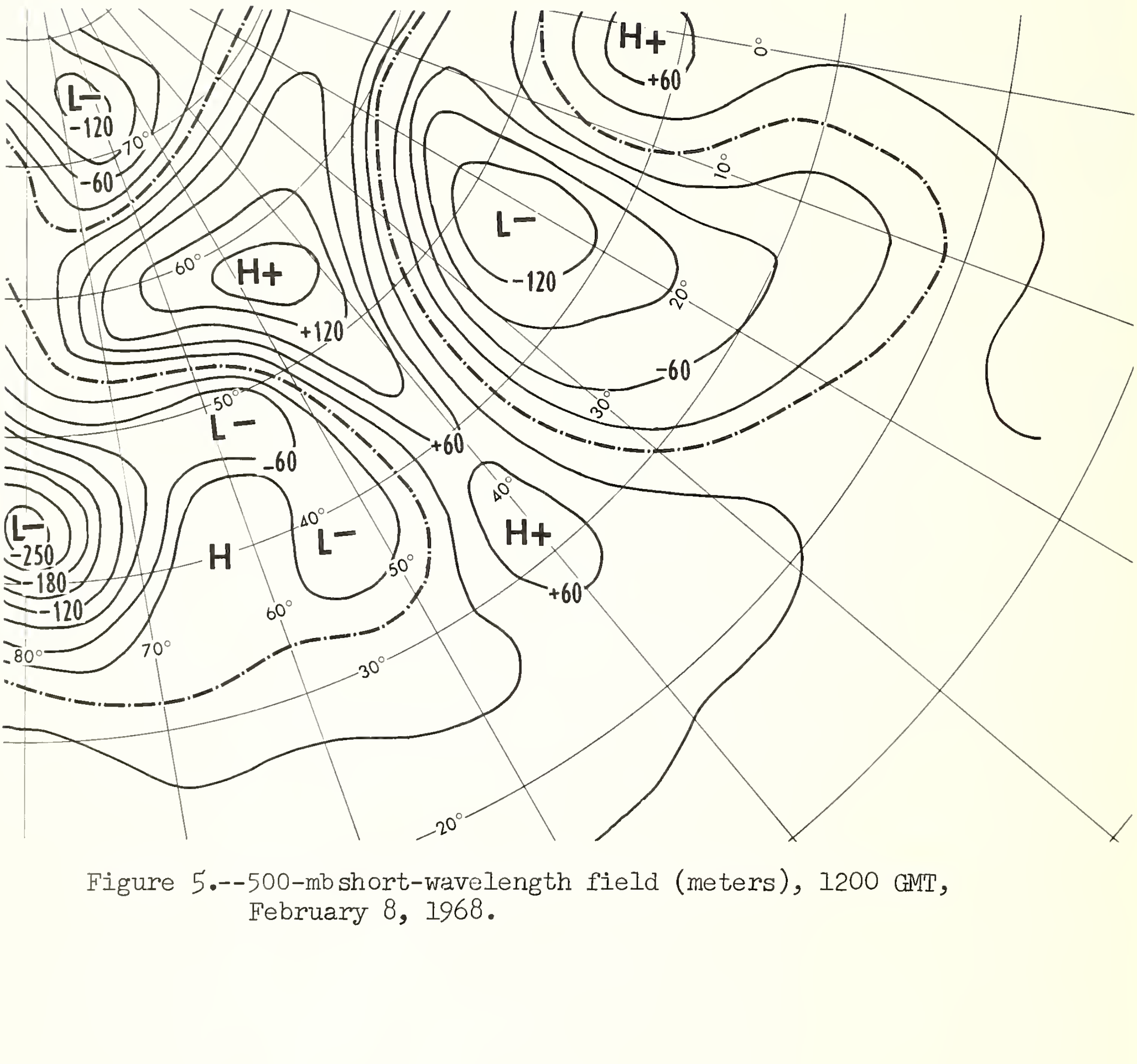

Figure 5.--500-mb short-wavelength field (meters), 1200 GMT, February 8, 1968.

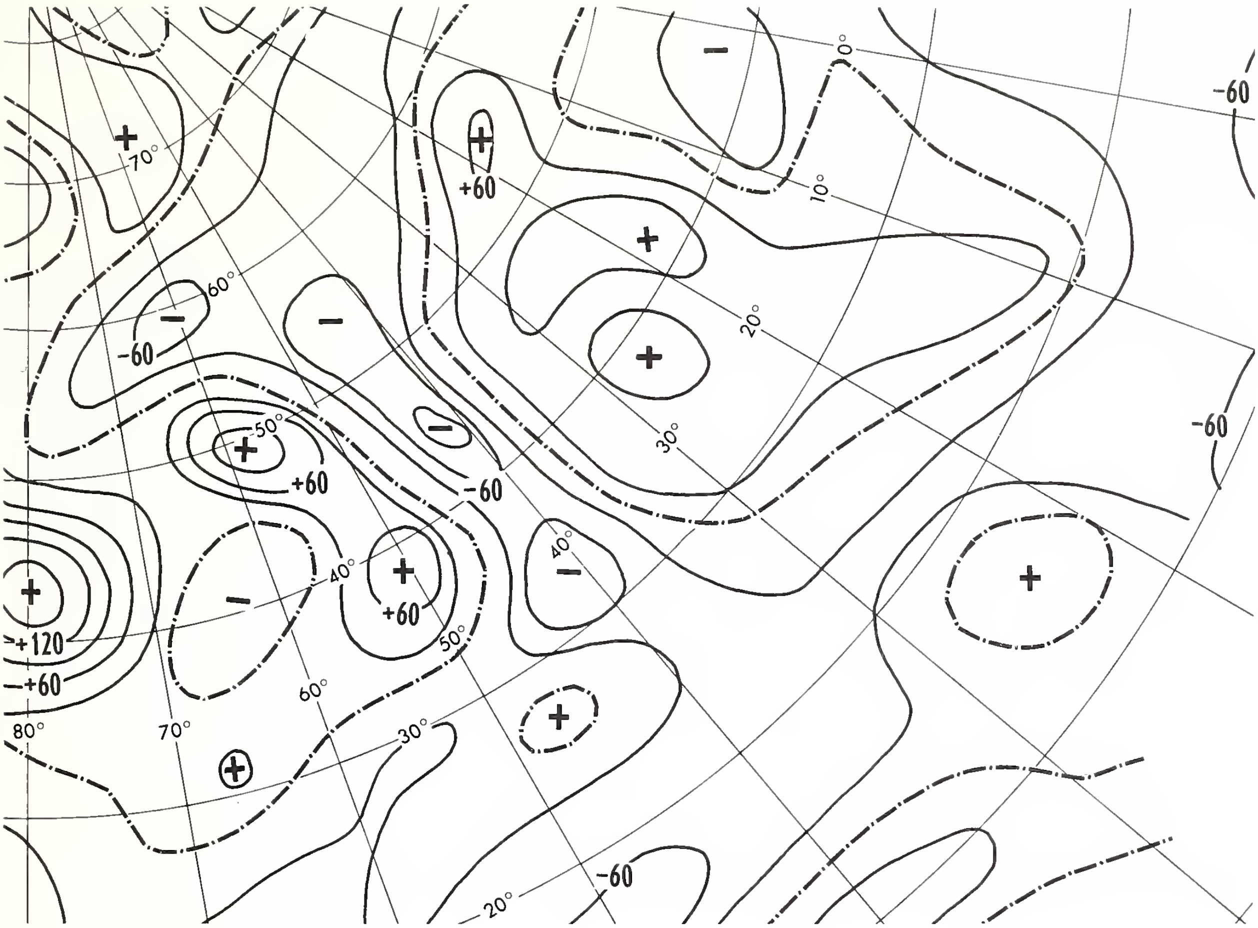

Figure 6.--500-mb relative vorticity field (x10^{-5} sec^{-1}), 1200 GMT, February 8, 1968.

By the mean value theorem for integrals:

$$Z_{SW} = -C\,a\nabla^2\, Z(a*) \tag{3}$$

where $Z(a*)$ represents the partially smoothed field at some degree of smoothing, $a*$, between 0 and a. The geostrophic relative vorticity q is given by

$$q = gf^{-1}\,\nabla^2\, Z_0 \tag{4}$$

where g is the acceleration of gravity and f is the coriolis parameter. Therefore, the correspondence between the relative vorticity and the short-wavelength component depends on the latitude and the equivalence of $\nabla^2 Z\,(a*)$ to $\nabla^2 Z_0$

Because the del square operator is wavelength dependent, there is no reason to expect direct proportionality between the magnitudes of the fields $\nabla^2 Z\,(a*)$ and $\nabla^2 Z_0$. Nevertheless, the patterns of these fields should be very similar. In particular, the locations where the fields have either extrema or zero values should be similar. Figures 5 and 6 are the relative vorticity and short-wavelength component fields for 1200 GMT, February 8, 1968. They show that the short-wave field retains, with light smoothing, the patterns of the relative vorticity field. Note that the short-wavelength field is opposite in sign from the vorticity field.

The correspondence found between identifiable cloud features and synoptic entities associated with specific details of the 500-mb relative vorticity field is illustrated in figure 7[2] and can be summarized as follows:

1. The boundaries of cellular convective cloud areas and the trailing edges of frontal cloud bands correspond to the zero lines in the relative vorticity field.

2. The locations of spiral cloud centers associated with cold-core systems correspond to positive vorticity maxima.

[2]The keying in figure 7 is applicable to all subsequent figures in this report.

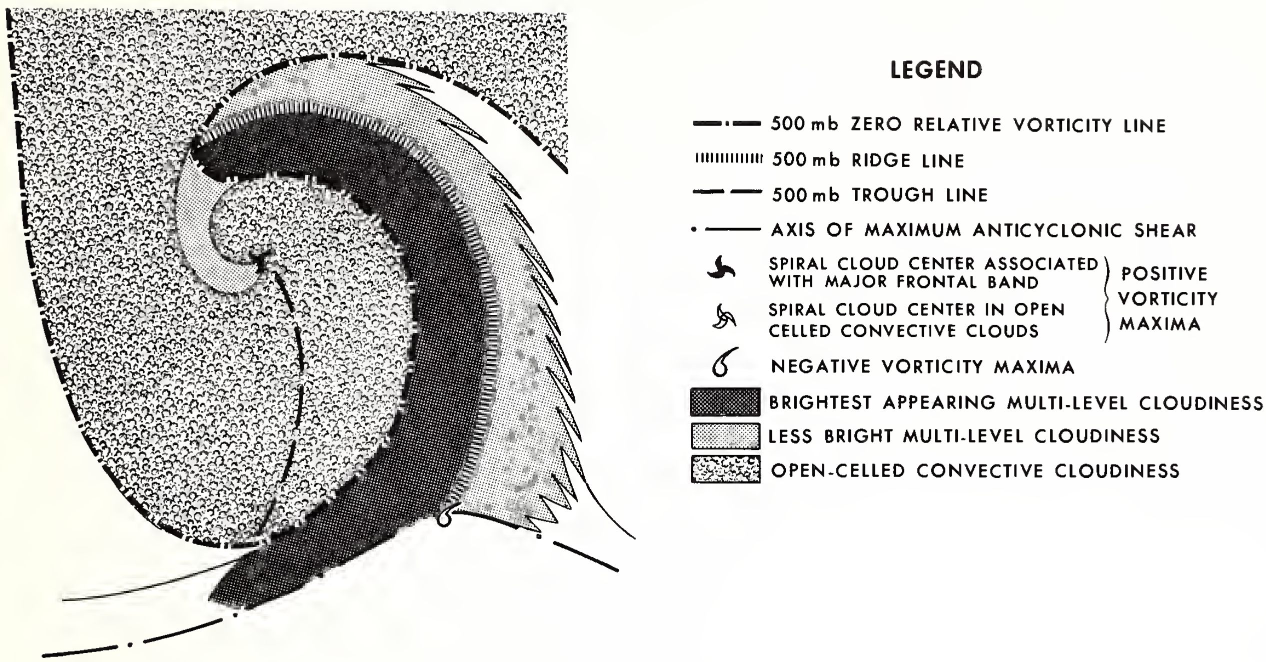

Figure 7.--Schematic representation of the relationships between cloud patterns and features of the 500-mb relative vorticity field.

3. The leading edges of frontal cloud bands correspond to axes of maximum negative vorticity.

4. The points marking the apex of the anticyclonic curvature on the leading edges of frontal cloud bands correspond to negative vorticity maxima.

These relationships permit a rather complete specification of the pattern of the short-wavelength field from an interpretation of the cloud patterns. It remains, however, to specify the magnitude of the negative extrema in the short-wavelength field.

4. STATISTICAL SPECIFICATION OF THE CENTRAL VALUES OF SHORT-WAVELENGTH SYSTEMS

A statistical investigation was undertaken to determine relationships between the magnitude of the negative maxima in the short-wavelength field and parameters derived from both the long-wavelength field and measurements of the cloud systems. The concept was to derive these relationships from a dependent sample over a relatively dense-data area so that the resulting regression equations could be used to specify the magnitude of systems over sparse data regions. The dependent data were derived over the North Atlantic Ocean, in the approximate region N. 25°-70°, E. 10°-W. 80°.

The cloud patterns were analyzed as follows (fig. 8). The location of a spiral cloud center was entered onto a 1:30,000,000 polar stereographic base map. A curved line was drawn radially outward from the center along the leading edge of the outermost cyclonically curved band (center to M'). In the eastern quadrant of the cloud pattern, the line was continued along the leading edge of the brightest-appearing cloudiness and merged with the leading edge of the frontal band. This line was continued along the frontal band to the point where the 500-mb trough line intersected the band (M' to T), i.e., to the point where the frontal cloud band either ends or changes abruptly in character. Next, a base line was drawn from the center to the point T, where the 500-mb trough intersected the cloud band. The length of this line is defined as the cloud amplitude. A second line was then drawn perpendicular to the base line at a location in which the distance along this second line through the leading and trailing edges of the curve depicting the cloud pattern was maximized. This line (M to M') is defined as the maximum diameter of the cloud system. Measurements of both cloud amplitude and maximum diameter were made in tenths of gridlengths. These measurements were obtained for each cloud system that could be associated with a specific maximum in the short-wave field. In addition to the cloud parameters, the following were computed at the location of each center: the latitude, the height value and the Laplacian of the long-wavelength field, the $\underline{u}$ and $\underline{v}$ component of the geostrophic wind (derived from the long wavelength

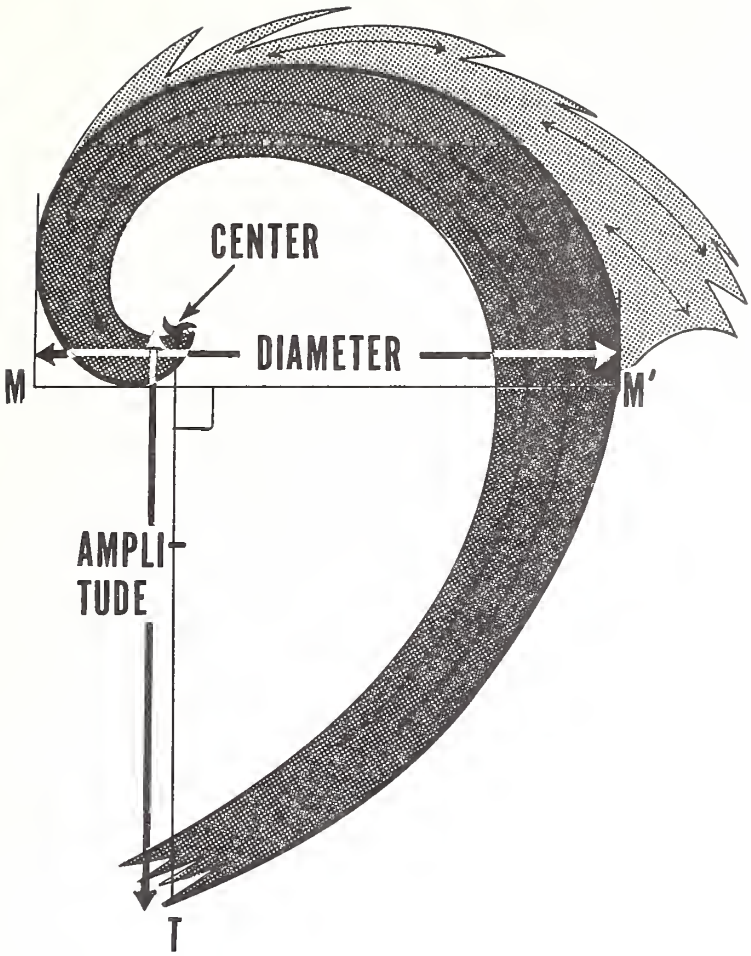

Figure 8.--Geometrical construction for determining the diameter and amplitude of a cloud system.

field), and the long-wave thickness advection. No attempt was made to classify the cloud systems by stage of development.

The dependent sample consisted of 156 cases over a 3-month period (February and October 1968 and June 1969). The population of cases was analyzed statistically by means of a stepwise linear regression screening procedure. After experimentation, the following predictors were selected for operational usage: latitude, the finite difference Laplacian of the long-wavelength field, and the maximum diameter and amplitude of the cloud system. These were chosen because they produced the greatest reduction of variance among the parameters which are most amenable for manual, operational use. A second regression equation with the cloud parameters excluded was derived from this sample. This equation is used when specification of the cloud parameters is ambiguous. The coefficients of the regression equations are provided in table 1.

Table 1.--Regression equation coefficients

Variable	With cloud parameters	Without cloud parameters
Constant	+21.5	-52.6
Latitude	-1.7	-0.8
Laplacian	-2.1	-2.5
Max diameter	10.4	
Amplitude	-1.0	

5. CONSTRUCTION OF 500-MB HEIGHTS AT THE LOCATION OF SPIRAL CLOUD CENTERS

Since parameters derived from the long-wavelength field are used in the regression equation for computing the intensity of the maxima in the short-wavelength field, and since the retrieval of absolute 500-mb heights requires the heights of the long-wavelength field, it must be assumed that the long-wavelength field is known. In a realtime operation the long-wavelength field derived from the current analysis is not available when the satellite observations are being interpreted. It is assumed that there is sufficient information in the 12-hour numerical forecast (the "first-guess" field) to allow the accurate specification of the long-wavelength pattern in the 500-mb height field. This assumption has been tested by determining the magnitude of the differences between the long-wavelength fields derived from first-guess fields and operational analysis fields.

The heights of the long-wavelength field as derived from the first-guess field and as derived from the analyzed fields were compared daily over a 3-month period. The same comparison was made for the Laplacian of the long-wavelength field. These comparisons were made over the North Atlantic. For each day in this sample, the following parameters were derived: The maximum and minimum values, the mean value, and the standard deviation. Also the correlation coefficient, the absolute maximum difference, and the root-mean-square (RMS) error between the first-guess field values and the analyzed values were computed. Tables 2 and 3 are statistics for each of the three months.

By applying the coefficients of table 1 to the corresponding values of tables 2 and 3 the errors involved in accepting the long-wavelength pattern derived from the first-guess field can be estimated. Applying worst-on-worst principles, the extreme error in the computed 500-mb heights at the location of the vorticity centers attributable to the errors in the long-wavelength field should be no greater than 80 meters. But considering the mean RMS errors, a more reasonable value for the expected error should be on the order of 20-30 meters. This is considered acceptably low for use in the current context.

By accepting the long-wavelength field derived from the first-guess field as a reasonable base, the 500-mb heights are retrieved by the direct addition of the two scale components.

The 500-mb heights at the location of the spiral cloud centers are obtained by interpreting the cloud patterns in terms of the parameters required in the solution of the regression equation (fig. 8). The Laplacian of the long-wavelength field is computed at the grid point closest to the location of the spiral cloud center. The central value of the associated short-wavelength system is then retrieved by solving the regression equation. Adding this value to the corresponding height in the long wavelength field produces the 500-mb height at the location of the spiral cloud center.

Where the short-wavelength field has a zero value (the zero line), the value of the long-wavelength is the 500-mb height. An example of this is illustrated in figure 9. As shown in figure 9 (left), the location of the zero line in the short-wavelength field is inferred from the cloud patterns. The zero line is superimposed upon the long-wavelength field, and 500-mb heights can be read at each intersection of the zero line with the contours of the long-wavelength field.

Table 2.--Statistics from comparisons of long-wavelength heights as derived from the "first guess" field and the analyzed 500-mb height field

	Extreme maximum	Monthly mean	Extreme minimum
	February 1968		
Absolute value (meters):			
Analysis	5924	5669	4836
Guess	5929	5677	4848
Standard deviation (meters):			
Analysis	307.3	241.1	175.0
Guess	296.8	236.0	168.4
Maximum difference (meters)	64.8	41.0	23.9
Correlation coefficient	.999	.998	.996
RMS error (meters)	22.4	16.2	6.6
	October 1968		
Absolute value (meters):			
Analysis	5933	5720	5161
Guess	5941	5723	5155
Standard deviation (meters):			
Analysis	215.5	178.3	127.7
Guess	211.4	177.5	128.4
Maximum difference (meters)	39.3	25.0	14.1
Correlation coefficient	.996	.989	.975
RMS error (meters)	15.0	10.3	5.6
	February 1969		
Absolute value (meters):			
Analysis	5896	5616	4941
Guess	5900	5618	4951
Standard deviation (meters):			
Analysis	247.1	201.0	150.0
Guess	239.0	197.6	148.4
Maximum difference (meters)	54.7	37.3	24.6
Correlation coefficient	.999	.998	.996
RMS error (meters)	21.5	14.8	7.9

Table 3.--Statistics from comparisons of the Laplacian of the long-wavelength height field as derived from the "first guess" field and the analyzed 500-mb height field

	Extreme maximum	Monthly mean	Extreme minimum
	February 1968		
Absolute value:			
Analysis	+85.0	+0.6	-50.9
Guess	+84.0	+1.9	-50.1
Standard deviation:			
Analysis	26.2	20.9	13.2
Guess	26.1	20.5	12.9
Maximum difference	11.5	8.2	5.2
Correlation coefficient	.998	.990	.979
RMS error	3.9	2.9	1.7
	October 1968		
Absolute value:			
Analysis	+63.4	-2.6	-22.7
Guess	+65.4	-2.5	-21.4
Standard deviation:			
Analysis	18.6	12.9	10.2
Guess	18.7	13.8	9.6
Maximum difference	10.4	5.8	3.0
Correlation coefficient	.996	.989	.975
RMS error	3.2	2.0	1.3
	February 1969		
Absolute value:			
Analysis	+80.0	-0.84	-22.1
Guess	+77.8	-0.98	-20.1
Standard deviation			
Analysis	20.8	17.2	13.2
Guess	20.5	16.4	11.7
Maximum difference	11.1	7.5	4.7
Correlation coefficient	.994	.987	.972
RMS error	3.7	2.8	2.0

6. VERIFICATION OF TECHNIQUE

The zero line values were verified for February 1968 over the area shown in figure 6. For each day the position of the zero line was inferred from the cloud photographs. Latitude-longitude locations along the zero line were noted at half-gridlength (NMC grid scale). At these locations values of the first-guess long-wave component field were compared to the total height indicated by the operational analysis. The same comparisons were made at locations taken from a "random" zero line. This line was drawn to represent the synoptic climatology of the area. Finally, at the locations taken from both the "inferred" and "random" zero lines the total height of the first-guess was compared to the final analysis. The results are presented in table 4.

Table 4.--Zero line verification for February 1968

	RMS discrepancy between inferred zero line heights and final analysis	RMS discrepancy between first-guess heights at inferred zero line locations and final analysis	Average gradient of final analysis at inferred zero line locations
	Meters	Meters	Meters per gridlength
"Inferred" zero line---	49	31	107
"Random" zero line-----	73	33	---

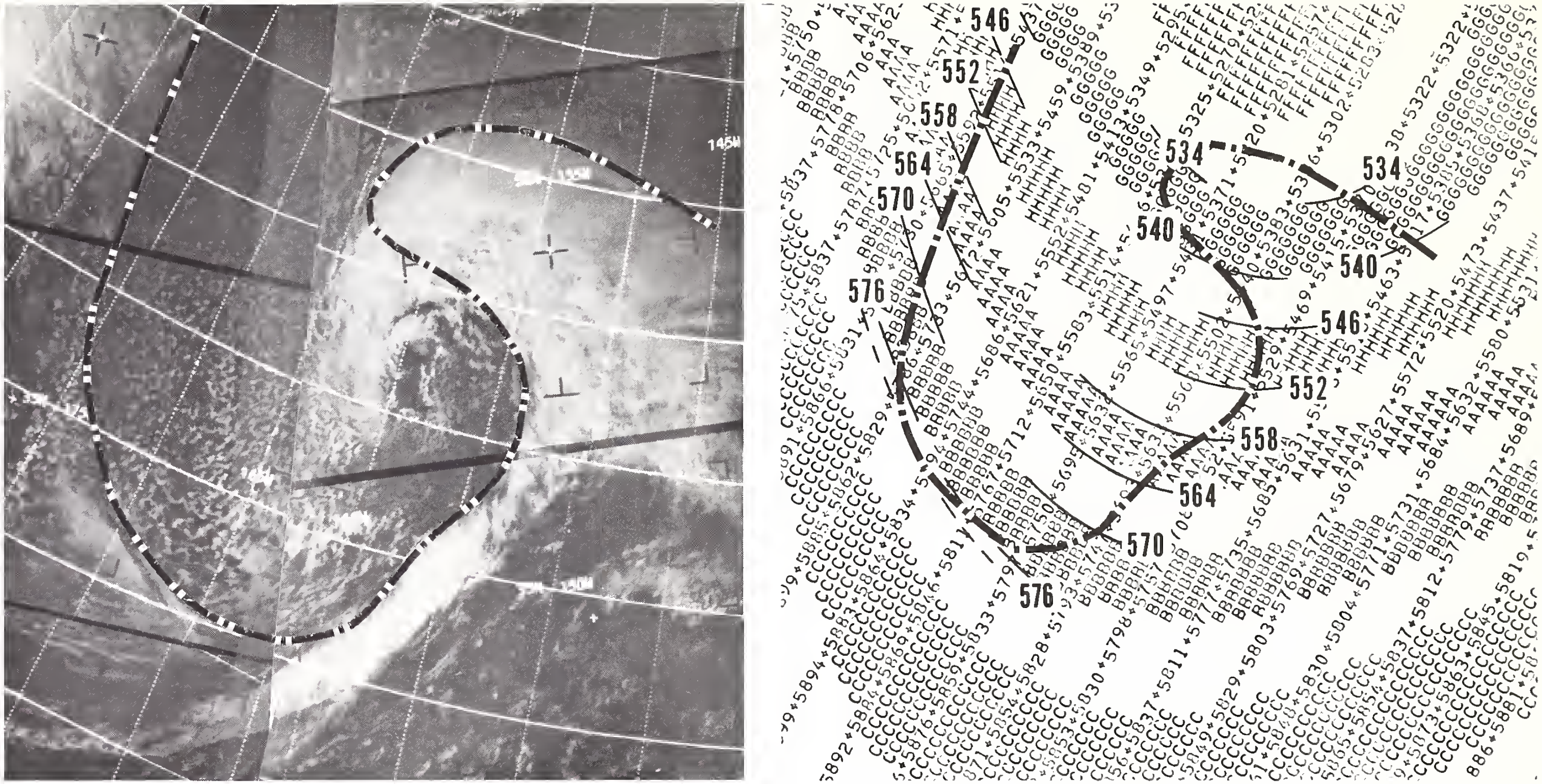

Figure 9.--Example of the method for determining height values along the inferred zero line in the relative vorticity field. <u>Left</u>, ESSA 9 cloud photographs and inferred zero line; <u>right</u>, inferred zero line superimposed on the long-wavelength height field.

The left-hand column of table 4 indicates the usefulness of the cloud photographs in determining the location of the zero line. The "inferred" zero line heights represent a considerable improvement over the "random" zero line heights. A more important question, however, is the accuracy of the "inferred" heights derived along the "inferred" zero line. Comparing the left and middle columns suggests that "inferred" heights are less accurate than the coincident values of the first-guess field, but the conclusion would be unwarranted. The National Meteorological Center's (NMC) objective 500-mb analysis, used as the verification standard, is biased toward the first-guess in inverse proportion to the amount of available data; and the area chosen for verification is not a dense data region. It is also apparent from the right-hand column in table 4 that the zero line occurs in areas of very tight gradient, and shifting a contour in the total height field by only half a gridlength is sufficient to explain the average discrepancy between the "inferred" heights and the final analysis. On this basis we believe the indicated difference between the "inferred" and analyzed heights to be within an acceptable range of uncertainty.

As shown in figure 10 and table 5, the magnitude of the discrepancy between zero line and analyzed height values is dependent on location relative to the cloud system. The region of largest discrepancies occurs in the main cloud shield. We found this to be caused by basic incompatibility between the scale of our interpretation of the zero line and the resolution of the analysis system. The tight curvature of the zero line suggested by the cloud patterns was not resolved on the grid used for objective analysis.

Table 5.--Zero line verification according to position within cloud system for "inferred" heights differing from the final analysis by at least 30 meters

Position	Ratio of estimates with discrepancy of 30 m or more to total sample	RMS error of estimates with discrepancy of 30 m or more
		Meters
Main cloud shield--------------------	154/242	83
Cold frontal band--------------------	52/290	60
Secondary development----------------	117/281	62
Boundary of open-celled convection---	282/1181	58

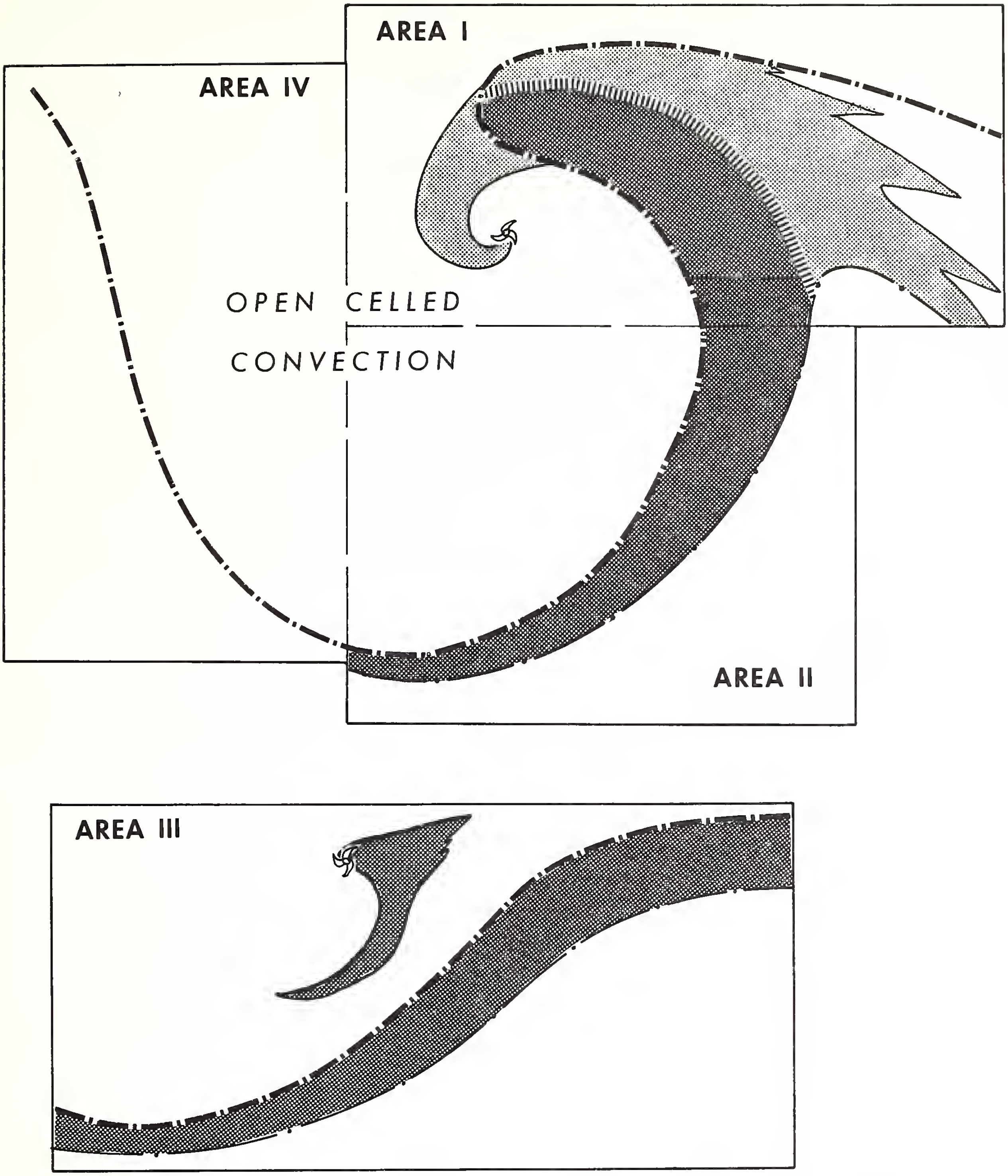

Figure 10.--Areas within cloud systems where the zero line heights were verified: Area I, main cloud shield; Area II, cold frontal band; Area III, secondary development; Area IV, boundary of open-celled convection.

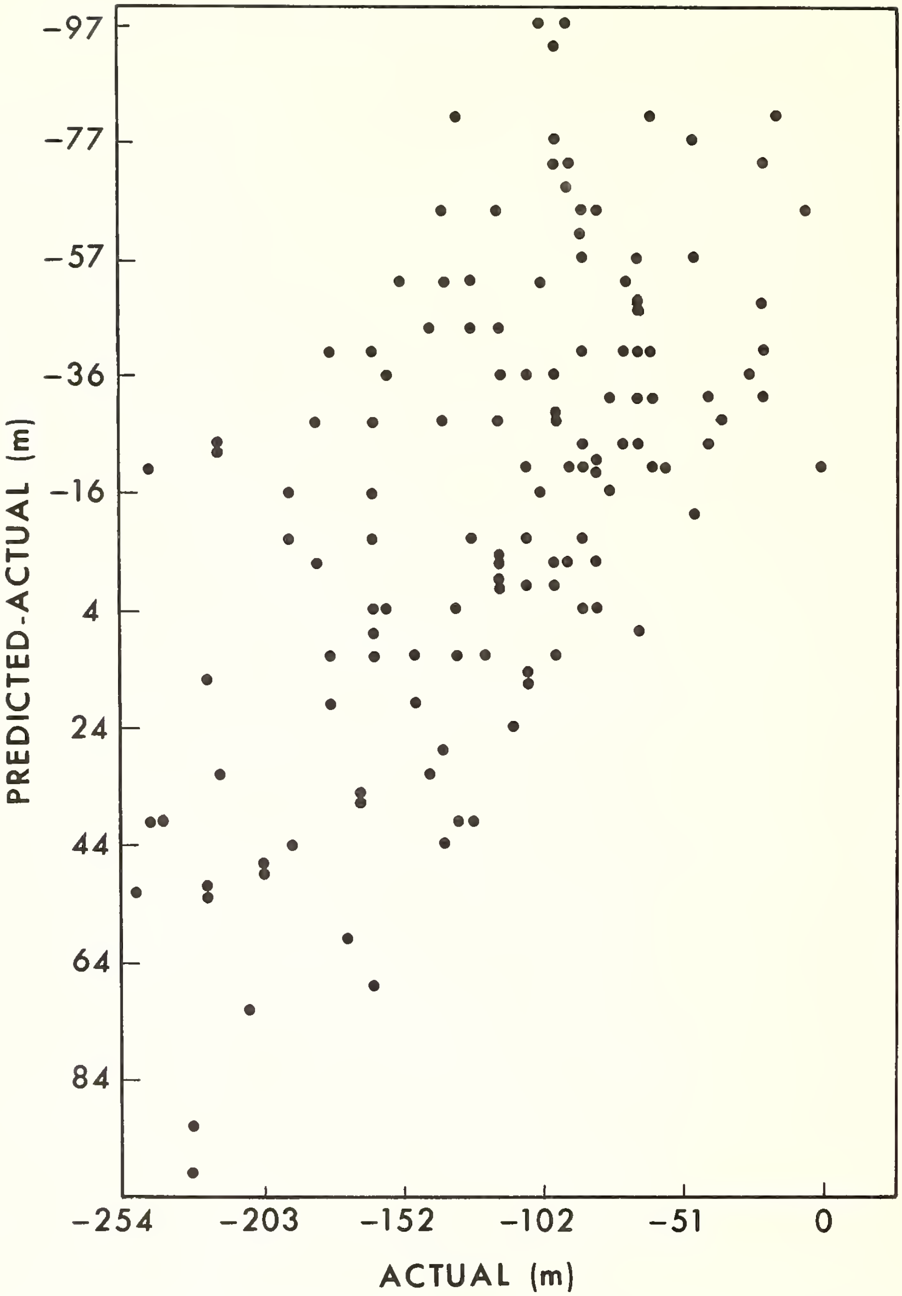

Figure 11.--Scatter diagram of the actual versus the residual of the intensity of the short-wavelength system.

The area where the second largest relative number of discrepancies occurs is in the region of secondary systems, such as vorticity centers in cold air or vorticity centers associated with enhancement of main frontal cloud bands (see Whitney and Herman, 1969). In these situations the accuracy of both the first-guess and final analysis fields is most suspect in sparse-data regions. Consequently, we feel that the zero line data are making their greatest contribution in these regions, even though the apparent error is large.

The regression equation for determining the negative extrema was verified with an independent set of data consisting of 131 cases from February, September, October, and November 1969. Results with the independent sample are compared to the dependent sample in table 6.

Table 6.--Regression equation and sample statistics for determining negative extrema of the short-wavelength field (meters)

Sample	Maximum	Minimum	Mean	Standard deviation	Regression error of estimate	Regression correlation coefficient
Dependent----	-20	-322	-139	61	38	.80
Independent--	-5	-248	-139	58	41	.72

Table 6 shows that the regression equation is stable. The accuracy of the heights derived from the regression equation is, as with the zero line heights, difficult to verify. The regression equation does produce some systematical error. A scatter diagram of the predicted minus the actual values versus the actual values for the independent sample is shown in figure 11. This diagram shows a consistent bias in the predicted values: the cases that are more intense than the mean are under-predicted, whereas those weaker than the mean are over-predicted. This appears to be characteristic of a least-squares fit to a sample of data, and efforts to correct for this bias have not shown appreciable success.

Appendix A provides the details adapting these techniques to a real-time operation and illustrates the outcome with three cases.

7. CONCLUSIONS

It has been demonstrated that quantitative use of satellite-observed cloud patterns can be made in modifying the 500-mb height field. The cloud pictures permit the identification and location of the short-wavelength systems in the 500-mb height field. Heights along the zero line(s) in the relative vorticity field are easily derived and demonstrate reasonable accuracy. The regression equations permit quantitative estimates of the magnitudes of the negative extrema in the short-wavelength field, and conversion of these values to absolute heights gives reasonable estimates of the 500-mb heights at the location of the spiral cloud centers. It is concluded that the technique can significantly improve the accuracy of the 500-mb height fields in sparse-data areas.

REFERENCES

Bradley, J. H. S., Hayden, C. M. and Wiin-Nielsen, A. C., "An Attempt to Use Satellite Photography in Numerical Weather Prediction," Final Report, Contract Cwb 11145, University of Michigan, Ann Arbor, Michigan, 1966.

Bristor, C. L., and Ruzecki, M. A., "TIROS I Photographs of the Midwest Storm of April 1, 1960," Monthly Weather Review, Vol. 88, No. 9-12 October-December 1960, pp. 315-326.

Brodrick, H. J., McClain, E. P., and Ruzecki, M. A., "Experimental Use of Satellite Pictures in Numerical Prediction, Part II," Meteorological Satellite Laboratory Report No. 36, ESSA, Washington, D.C., 1966.

Fjortoft, R., "On a Numerical Method of Intergrating the Barotropic Vorticity Equation," Tellus, Vol. 4, No. 3, March 1952, pp. 179-194.

Holl, M. M., "A New Version of the Beta Program for an 89x89 Grid," Technical Note No. 1, Contract N00228-67-C-2759, Meteorology International Inc., Monterey, Calif., 1967.

Holl, M. M., "Scale and Pattern Spectra and Decompositions," Technical Memorandum No. 3, Contract N228-(62271) 60550, Meteorology International Inc., Monterey, Calif., 1963.

McClain, E. P., Ruzecki, M. A., and Brodrick, H. J., "Experimental Use of Satellite Pictures in Numerical Prediction," Monthly Weather Review, Vol. 93, No. 7, July 1965, pp. 445-452.

Nagle, R. E., and Clark, J. R., "An Approach to the SINAP Problem: A Quasi-Objective Method of Incorporating Meteorological Satellite Information in Numerical Weather Analyses," Final Report, Contract E-93-67(N), Meteorology International Inc., Monterey, Calif., 1968.

Nagle, R. E., Clark, J. R., Holl, M. M., and Reigel, C. A., "Objective Assembly of Meteorological Satellite Information," Final Report, Contract N62306-1775, Meteorology International Inc., Monterey, Calif., 1966.

Whitney, L. F., and Herman, L. D., "The Nature of Intermediate-Scale Cloud Spirals," National Environmental Satellite Center Technical Report No. 45, ESSA, Washington, D.C., 1968

Widger, W. K., "A Synthesis of Interpretations of Extratropical Vortex Patterns as Seen by TIROS," Monthly Weather Review, Vol. 92, No. 6 June 1964, pp. 263-282.

APPENDIX A

Application

At present, these zero-line and regression techniques are being applied only to the 0000 GMT analysis in the area covering the North Pacific Ocean from about the International Date Line to the west coast of North America. The 12-hour numerical 500-mb height forecast from the previous 1200 GMT analysis is computer processed to produce the short- and long-wavelength fields. These products are available to the analyst at about 2200 GMT. The primary satellite data used are Automatic Picture Transmission System (APT) pictures of cloud patterns over the eastern and central Pacific Ocean. These data received from the satellite at San Francisco and Hawaii, are relayed directly to the National Environmental Satellite Center (NESC), Suitland, Md. Although these data provide adequate coverage to perform the analyses, they are from 3 to 6 hours earlier than the 0000 GMT analysis time. This is partially compensated for by use of 2300 GMT data from the geosynchronous Applications Technology Satellite, ATS 1. A preliminary analysis is performed using the APT data and then adjusted by using the ATS 1 observation.

The 500-mb heights at the spiral cloud centers and along the zero line(s) are derived and plotted on a 1:20,000,000 polar stereographic map. The locations of troughs, ridges, and the axes of maximum anticyclonic shear inferred from the cloud patterns also are entered on this map. Using the derived 500-mb heights, the synoptic features indicated above, and the general configuration of the cloud patterns, the analyst constructs a contour height analysis for the area.

The completed analysis is given to the Automated Analysis Branch of NMC at approximately 0100 GMT; these data are then blended with the 0000 GMT radiosonde observations through NMC's 500-mb hand analysis. The final hand analysis is compared to a preliminary machine analysis (the RADAT analysis), and NMC analysts generate "bogus" wind and height reports to correct the discrepancies. These "bogus" heights are entered into the operational machine analysis which is used as the initial data for the Primitive Equation Model forecast.

Satellite Input to Numerical Analysis and Prediction (SINAP) has been used daily since July 1, 1969. This section illustrates several examples of the operational product.

0000 GMT October 16, 1969

Figure 12, top, shows the ESSA 9 digitized mosaics for approximately 0000 gmt, October 16, 1969. Superimposed on the mosaic are the first-guess field, 500-mb contours, and the zero line of the short-wavelength field as derived from the first-guess field. The discrepancies between

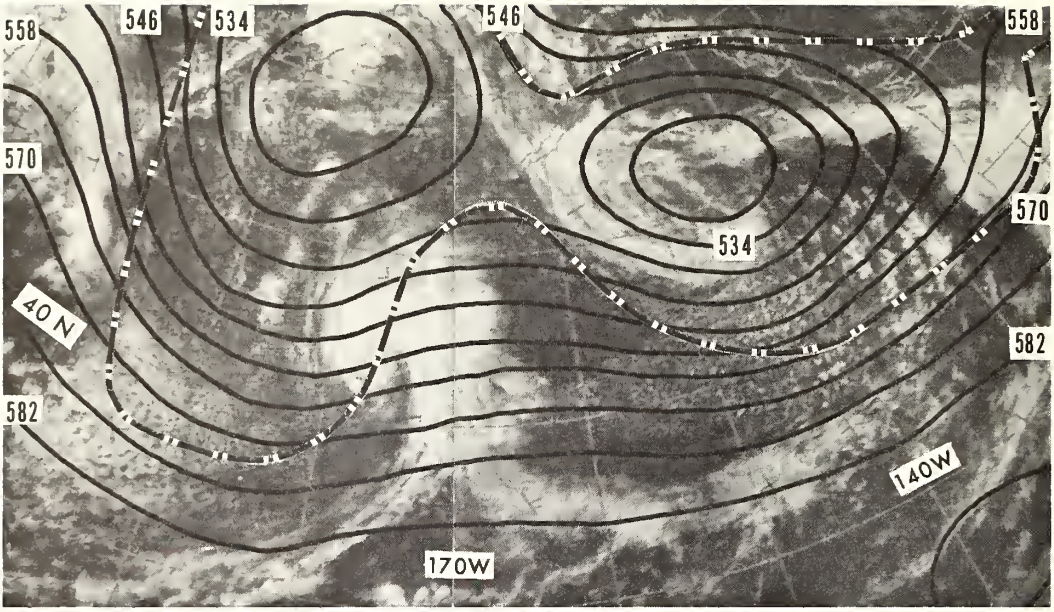

Digitized cloud mosaic, 500-mb first-guess contours (decameters) and short-wavelength field zero line.

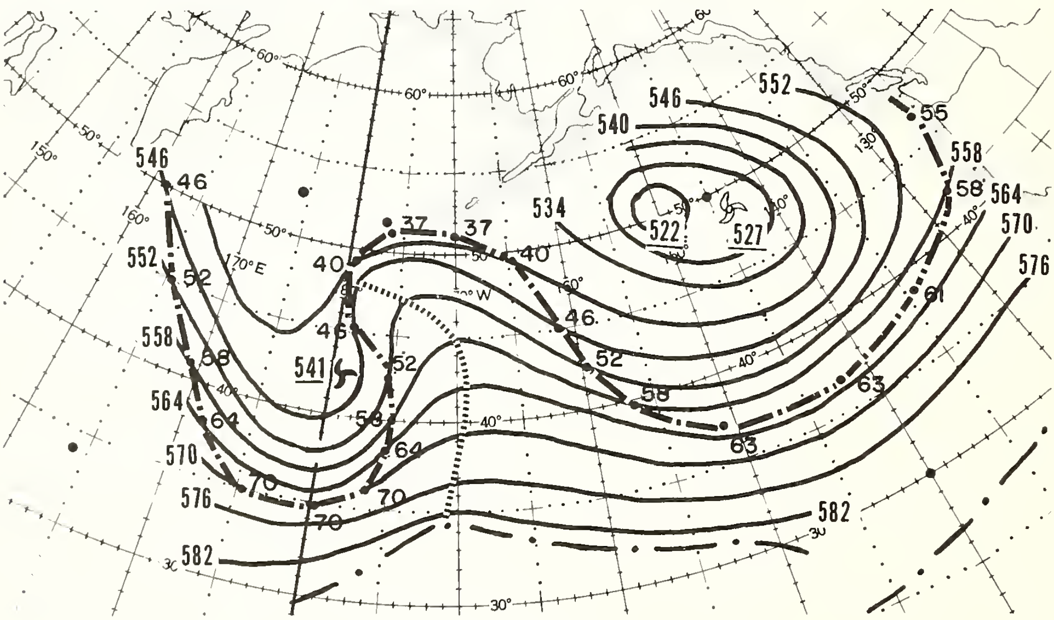

SINAP analysis

Figure 12.--Cloud pattern, numerical fields, and SINAP analysis for 0000 GMT, October 16, 1969.

the zero line and the cloud patterns shown in the figure are rather typical. The general pattern of the zero line reflects the systems which appear in the cloud patterns, but there are errors in location and amplitude. For example, the ridge line near 170° W. appears too far east compared with the cloud patterns. Near 40° N. and 165° E. the zero line incorrectly extends through an area of inversion-dominated stratocumulus clouds. Near 40° N., 150° W., the zero line is incorrectly located in the middle of a field of open-celled convective cloudiness. the SINAP analysis for 0000 GMT, October 16, 1969 is shown in figure 12, bottom. This analysis contains the heights along the zero line (in decameters with the first digit deleted) and at three vorticity centers computed from the regression equation (decameters). The height at the vorticity center located near 44° N., 179° W. was 5,410 meters; this value differed from the first-guess field by -150 meters. Heights at the two vorticity centers located near ship PAPA (50° N., 145° W.) were 5,220 meters and 5,270 meters. These heights deviated from the first-guess field by about -60 meters.

In figure 13, top, the 500-mb contours from NMC's hand analysis are superimposed upon the ESSA 9 digitized mosaic. Also shown is the zero relative vorticity line derived from the machine analysis for 0000 GMT, October 16, 1969. A reasonable correspondence between the cloud patterns and the zero relative vorticity line is apparent, although improvements could still be made. (Note that the zero line still encloses a large area of stratocumulus near 40° N., 175° E.)

In figure 13, bottom, the SINAP heights are shown together with the available 500-mb wind and height reports. Note that the zero line heights near radiosonde stations appear quite compatible with the reported heights. In particular, the location of the zero line and its derived heights is completely compatible with the apparent location of the jet stream as indicated by the wind speed at the station on the east coast of Kamchatka Peninsula. No data are available to verify the system located near 44° N., 179° W.; the height at the vorticity center located near 50° N., 150° W., however, was compatible with the observed height and wind at ship PAPA.

0000 GMT, February 9, 1970

The previous case represents a classical example where the distinct change between cloud types leaves little doubt as to the proper location of the vorticity features. This is usually the exception rather than the rule; consequently, the analyst must make subjective decisions as to the locations of the zero line and the vorticity centers. This example and the next were chosen at random from the daily operational analyses. The complex cloud patterns of these cases represent the usual conditions which confront the analyst. The SINAP analyses shown have been slightly modified from the operational product primarily for esthetic purposes,

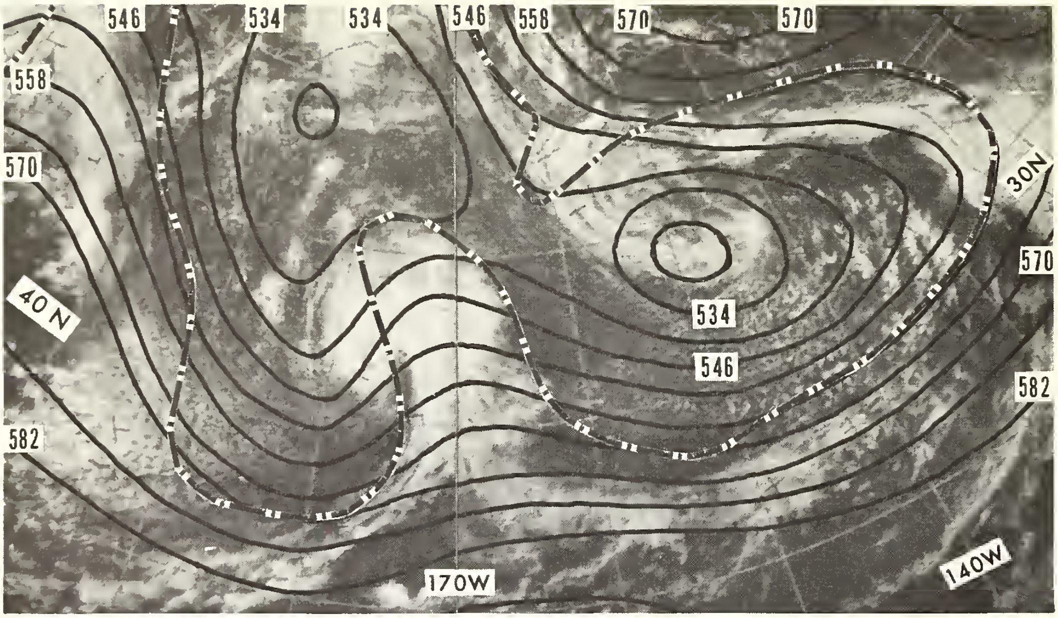

Digitized cloud mosaic, NMC's operational 500-mb analysis and 500-mb relative vorticity zero line

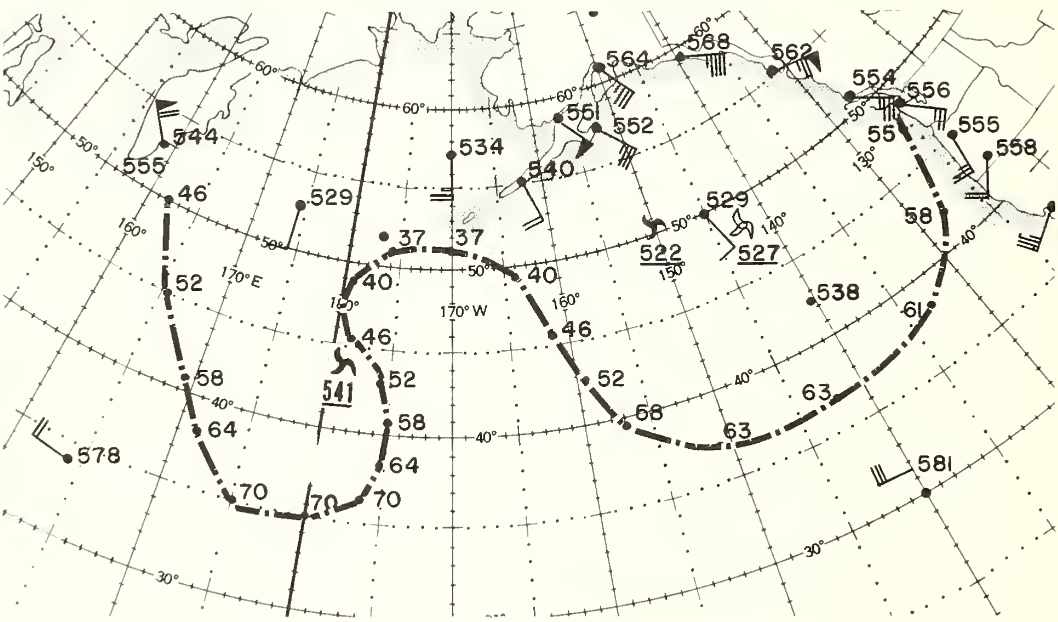

SINAP heights and radiosonde data

Figure 13.--NMC's operational analysis, SINAP heights, and radiosonde data for 0000 GMT, October 16, 1969.

but also to insure registration with the digitized ATS-1 photograph[3]; they differ only in minor details from the operational products which were produced independently of the radiosonde data.

Figure 14, top, shows the first-guess 500-mb height contours and the zero line in the short-wavelength field for 0000 GMT, February 9, 1970, superimposed on the 2130 GMT, February 8, 1970, ATS-1 digital product. The first-guess field in this case shows good agreement with the large-scale pattern of the cloudiness, but contains no information on the short-wavelength systems indicated by the cloud patterns. Conspicuous by its absence from the contour field is the vorticity maximum indicated by the intense vortical cloud pattern located near 42° N., 160° W. Another deficiency in the first-guess field is the trough which connects the deep low centered near 50° N., 175° W. to the subtropical system located near 35° N., 135° W. The presence of this trough places the area N. 40°-50° and W. 135°-155° under a positive vorticity regime, whereas the cloud patterns indicate the opposite.

The SINAP analysis is shown in figure 14, bottom. Three vorticity maxima were entered into the SINAP analysis which were not present in the first-guess field. These systems were located near 40° N., 175° W.; 42° N., 160° W.; and 26° N., 130° W. The heights computed at these centers deviated from the first-guess field by -60, -60, and +40 meters respectively. In the SINAP analysis the pattern of the positive vorticity was separated into two separate pools; one associated with the deep low in the Central Pacific and the second with the cut-off low west of California. Strong ridging and negative vorticity were indicated in the region where the first-guess field indicated a trough. Another area where considerable adjustment was indicated was near 30° N., 175° W.; here the first-guess field zero line was adjusted some 5 degrees to the south.

The operational 500-mb height analysis and the zero relative vorticity line derived from it are shown superimposed upon the ATS-1 digitized pictures in figure 15, top. It is clear that many details of the SINAP analysis have been incorporated into NMC numerical product. A secondary center has been entered into the analysis in the southeast quadrant of the cut-off low in the Eastern Pacific. A sharp short-wavelength system has been analyzed near 45° N., 155° W. which corresponds reasonably with the cloud patterns. Of primary importance is the ridge which has been entered into the analysis along 145° W.; this has effected a reversal in the sign of the vorticity of the first-guess field in this area. The zero line between 150° W. and 160° W. shows some noise; but with gradients of the magnitude indicated by the analysis in this area, very subtle changes in

[3]This picture is produced daily from the 2130 GMT ATS-1 cloud photograph. The cloud photograph is processed by machine and remapped in full resolution on a 1:20,000,000 polar stereographic projection.

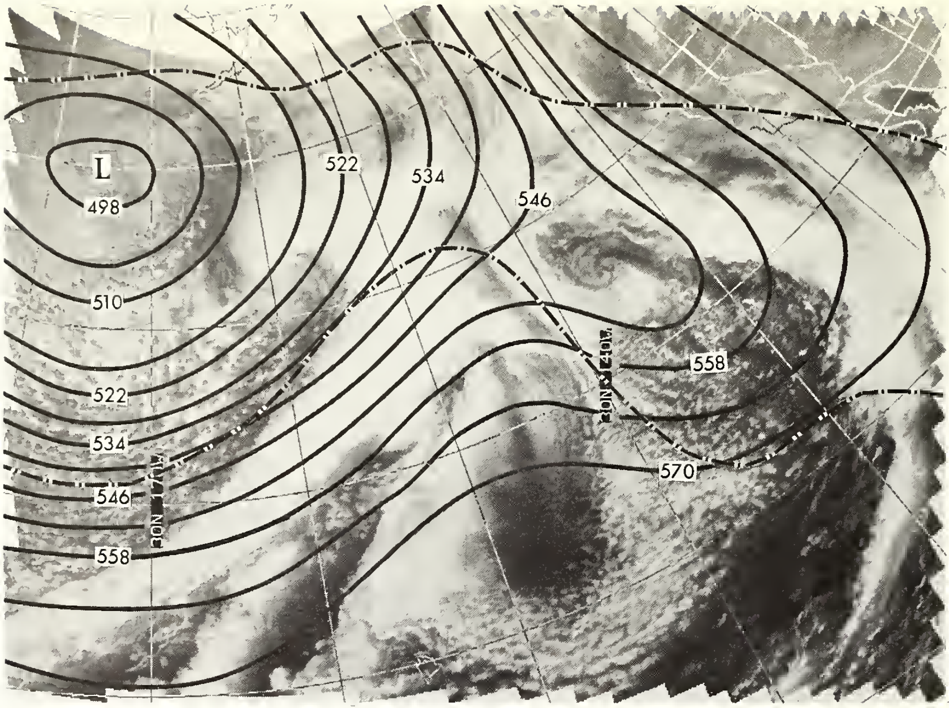

Digitized cloud photograph, 500-mb first-guess contours (decameters) and short-wavelength field zero line

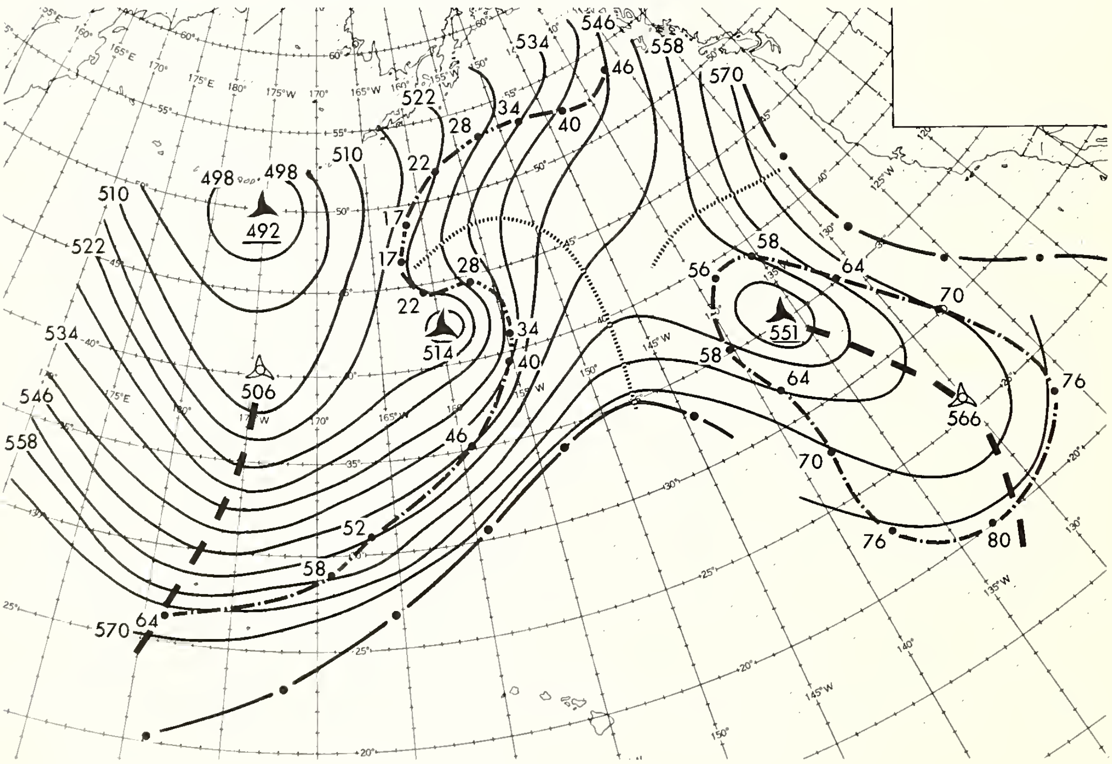

SINAP analysis

Figure 14.--Cloud pattern, numerical fields, and SINAP analysis for 0000 GMT, February 9, 1970.

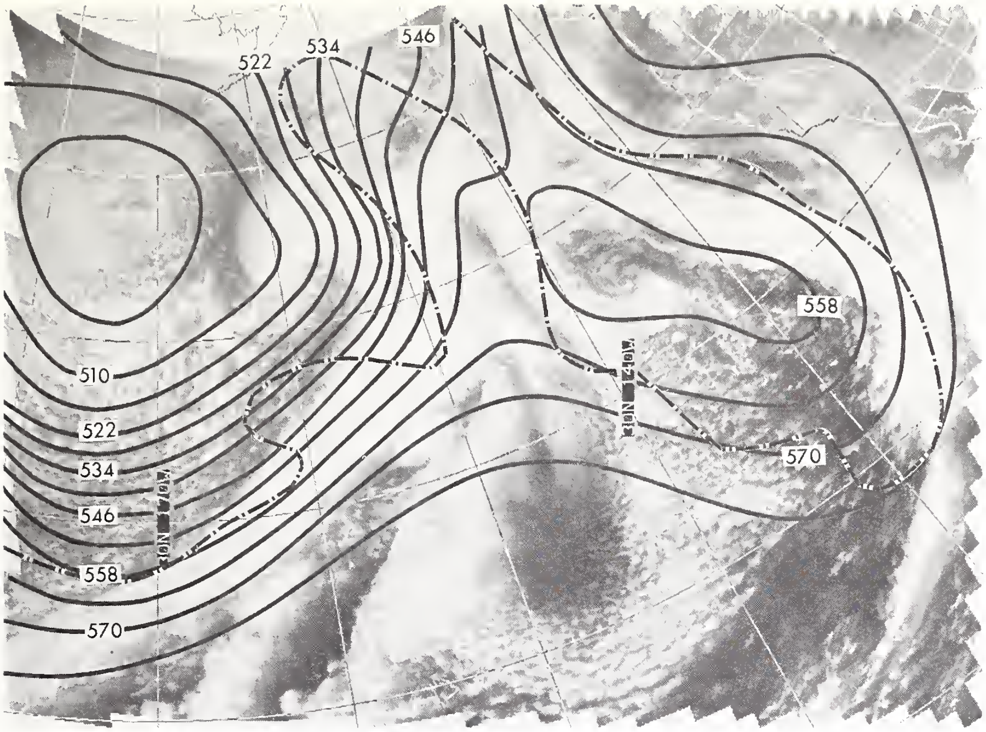

Digitized cloud photograph, NMC's operational 500-mb analysis and 500-mb relative vorticity zero line

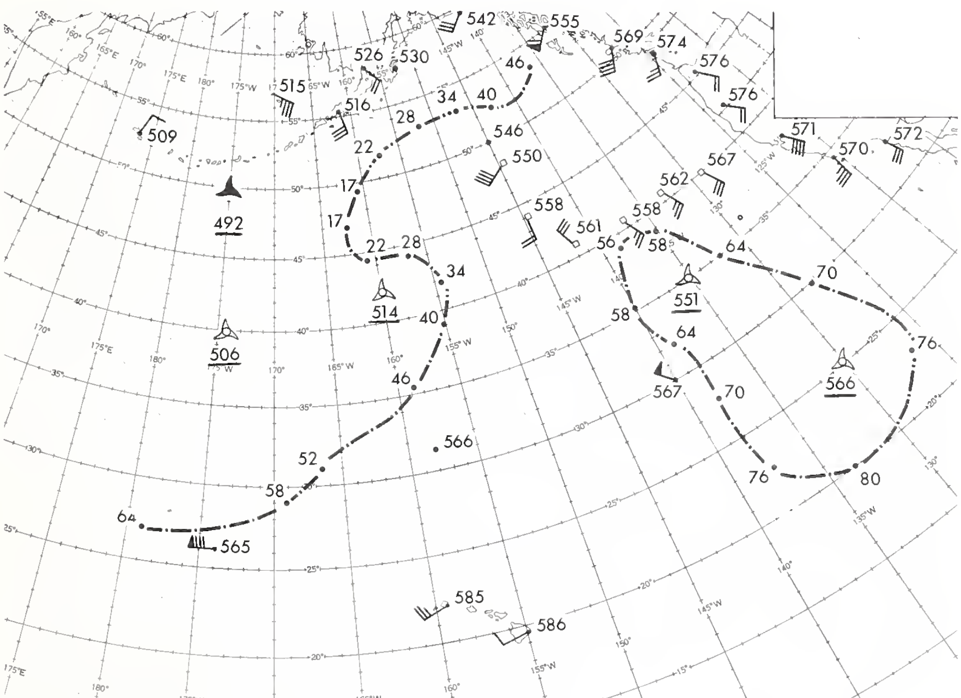

SINAP height and radiosonde data

Figure 15.--NMC's operational analysis, SINAP heights, and radiosonde data for 0000 GMT, February 9, 1970.

the curvature of the contours can produce large changes in the corresponding vorticity field. This noise is considered of negligible significance.

The SINAP heights and the actual radiosonde and reconnaissance data are shown in figure 15, bottom. With the exception of one area, the heights along the zero line and at the vorticity centers appear perfectly compatible with the reported heights. The SINAP heights along the trailing edge of the cloud band associated with the cut-off low are consistently too high. This is a factor that has been observed consistently in the presence of intense convective cloud bands associated with this type of system. Placing the zero line along the leading edge of such a cloud band produces heights which are much more compatible with observations.

0000 GMT, March 23, 1970

The 500-mb first-guess height field and the zero line in the short-wavelength field are shown superimposed upon the ATS-1 digitized product for 2130 GMT, March 22, 1970 in figure 16, top. As in the previous cases, the contour pattern in the first-guess field and the location of the zero line correspond reasonably with the cloud patterns. In this case the major deficiency in the first-guess field is the lack of amplitude in the short-wavelength systems.

The satellite photographs at this time showed an intense "comma" shaped cloud pattern at 44° N., 179° E. The SINAP analysis in figure 16, bottom, correctly included this cloud pattern entirely within the area of positive vorticity. This bright comma-shaped cloud pattern is associated with an area of strong positive vorticity advection within the cold air in advance of the 500-mb trough line. The northward bulge of the frontal band in the vicinity of 45° N., 160° W., indicates the vorticity maximum is interacting with the primary baroclinic zone. In such transition situations the location of the zero line in the area of interaction is not always distinct, but the correct analysis is to place the zero line along the northwest boundary of the dense cirriform cloudiness associated with the frontal band. The sag in the contours located near 33° N., 175° W. in the first-guess field produced a marked disagreement between the cloud patterns and the first-guess field zero line. The clouds show that this feature was erroneous; it was eliminated in the SINAP analysis.

NMC's operational 500-mb height analysis for 0000 GMT, March 23, 1970 and the corresponding zero relative vorticity line are shown superimposed upon the 2130 GMT, March 22, 1970, ATS-1 digitized picture (figure 17, top). Comparing the contour patterns of figures 16 and 17 reveals that the operational analysis contains much more detail than was evident in the first-guess field. The enhancement of the gradients in the operational analysis is particularly apparent compared with the first-guess field.

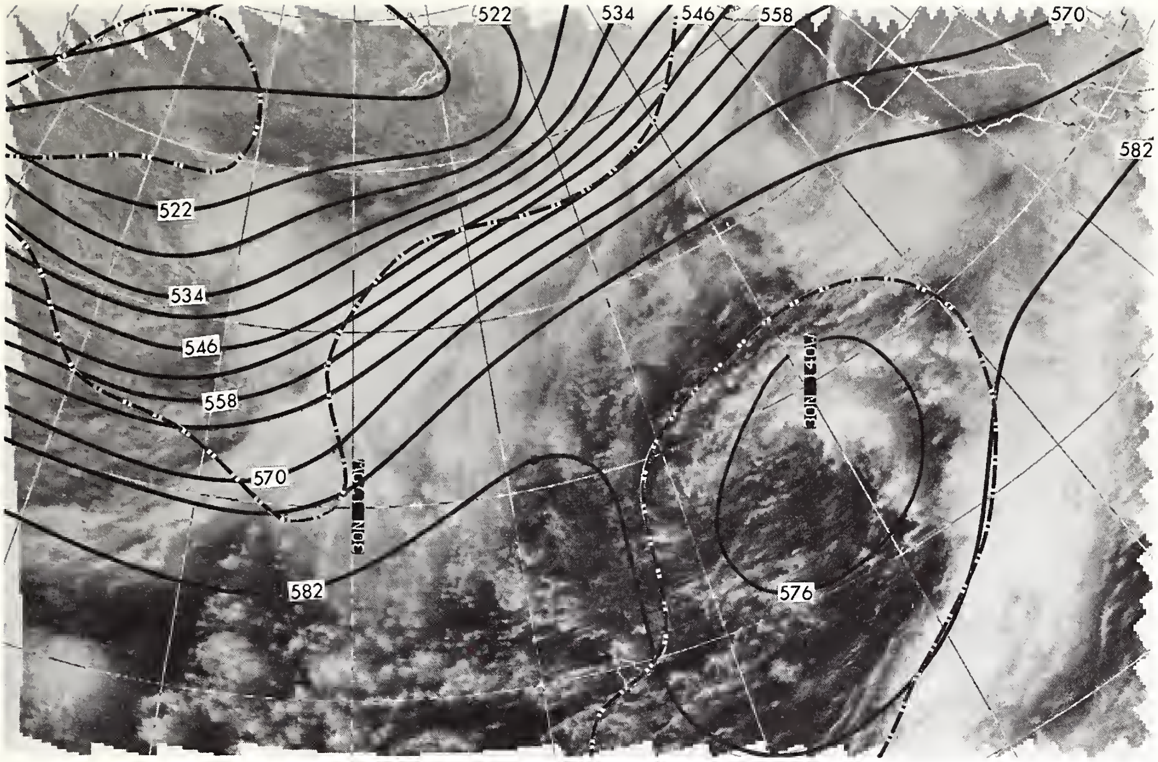

Digitized cloud photography, 500-mb first-guess contours (decameters) and short wavelength field zero line

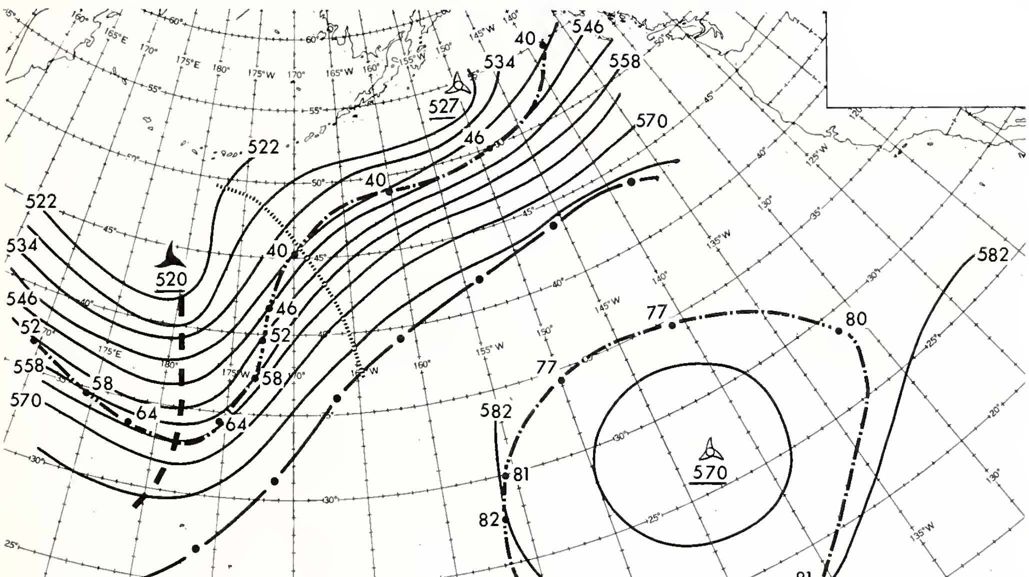

SINAP analysis

Figure 16.--Cloud patterns, numerical fields, and SINAP analysis for 0000 GMT, March 23, 1970.

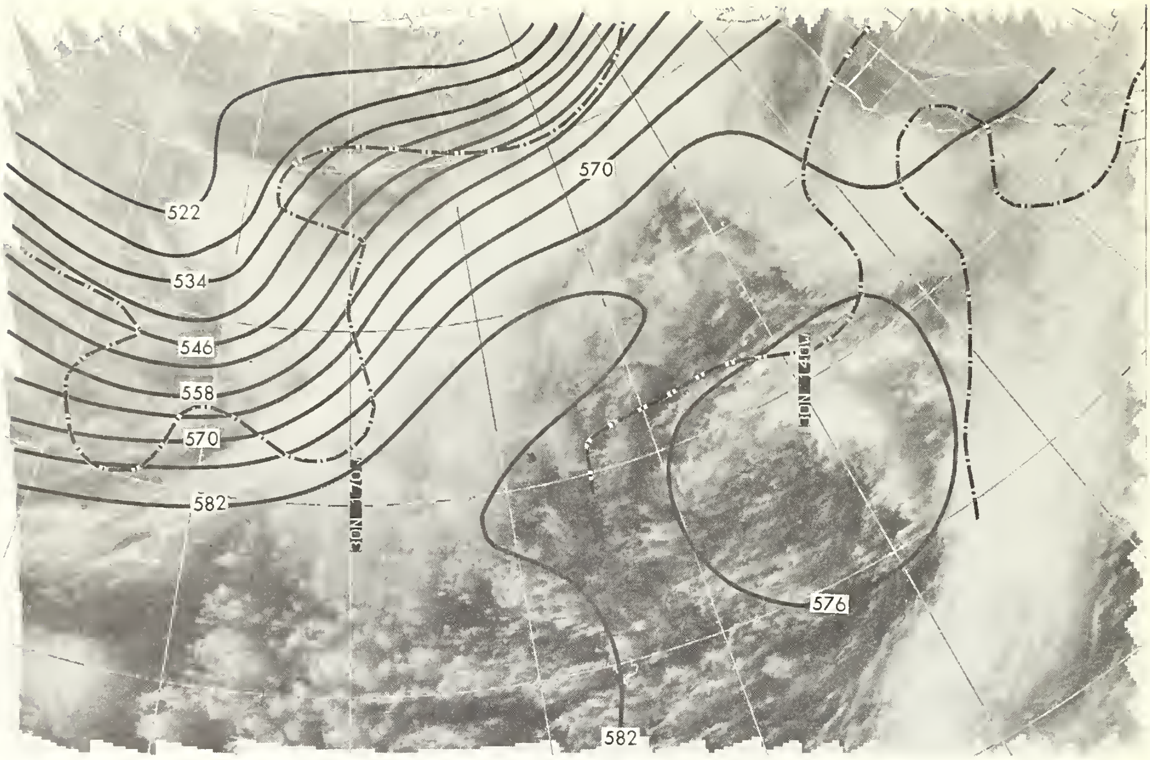

Digitized cloud photograph, NMC's operational 500-mb analysis and 500-mb relative vorticity zero line

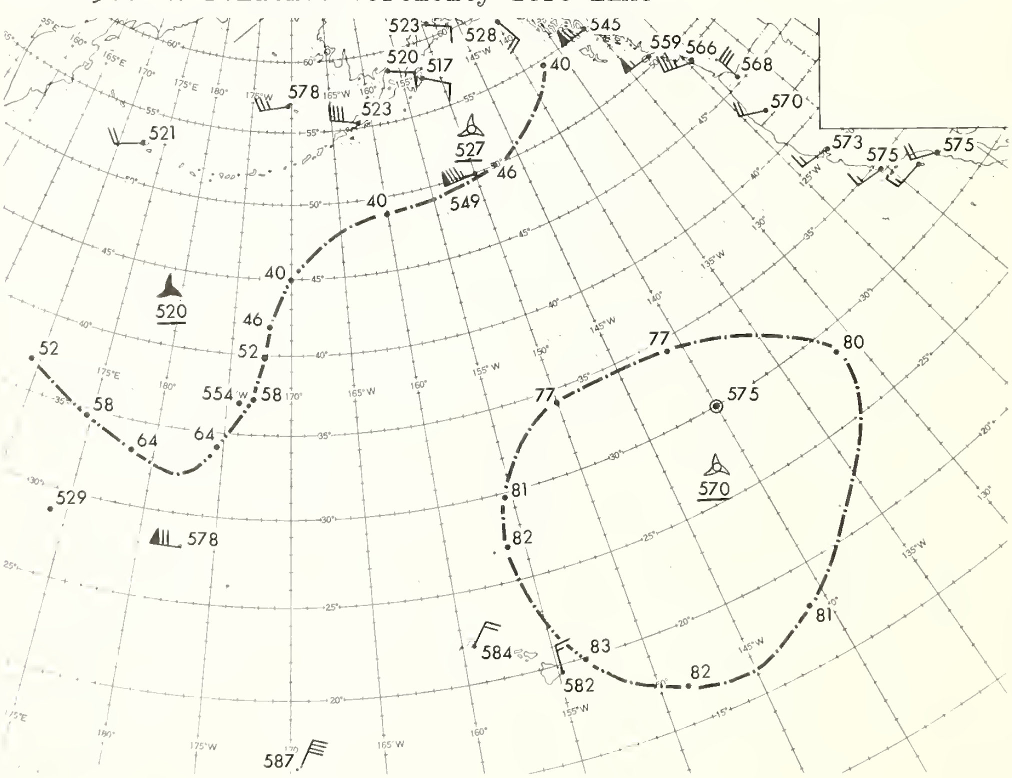

SINAP heights and radiosonde data

Figure 17.--NMC's operational analysis, SINAP heights, and radiosonde data for 0000 GMT, March 23, 1970.

The zero relative vorticity line as derived from the operational height analysis is very noisy, however; and the analysis still contains the erroneous area of positive vorticity centered near 35° N., 172° W. This is attributed to an excess of cyclonic curvature of the contours in this area.

In figure 17, bottom, are the heights derived from the SINAP analysis, together with the available radiosonde data for 0000 GMT, March 23, 1970. There are only three points where the SINAP data were sufficiently close to radiosonde reports to allow direct comparison of the heights. The height along the zero line 2 degrees east of ship PAPA was 5,460 meters; the reported height at PAPA was 5,490 meters, and the wind was 260° at 85 knots. A height of 5,830 meters was derived along the zero line some 2° east of Hawaii; this was 10 meters higher than the reported height at Hilo. A height of 5,700 meters was computed at the open vortex located at 27° N., 142° W.; this appears consistent with the height reported by ship NOVEMBER (30° N., 140° W).

APPENDIX B

Properties of Scale Separation

The smoothing filter is defined by

$$\phi \equiv \phi_0 + \delta^2 \int_0^a \nabla^2 \phi \, da \tag{B1}$$

where ϕ is the smoothed field, ϕ_0 is the original field, δ is a constant, and a is the degree of smoothing parameter. For purposes of later generalization it is convenient to express equation (B1) in operator notation:

$$\phi[a] = \phi[0] - \phi[0, a] \tag{B2}$$

where $\phi[a]$ is to be read as "the field ϕ smoothed to degree of smoothing a," and $\phi[0, a]$ is to be read as "the residual field resulting from smoothing the ϕ field from the state $a = 0$ to $a = a$."

In order to investigate the properties of the smoother, let us assume that the field ϕ is represented by a one-dimensional wave with wave number k. The amplitude of the wave will be a function of the degree of smoothing. In differential form equation (B1) is given by

$$\frac{\partial \phi}{\partial a} = \delta^2 \nabla^2 \phi \tag{B3}$$

and the one-dimensional wave is expressed by

$$\phi[0] = A_k[0] e^{ika} \tag{B4}$$

Substituting (B4) into (B3) and solving gives

$$\phi[a] = \phi[0]\, e^{-k^2 \delta^2 a} \tag{B5}$$

$$A_k[a] = A_k[0]\, e^{-k^2 \delta^2 a} \tag{B6}$$

The amplitude reduction factor caused by the smoothing is given by

$$R = \frac{A_k[a]}{A_k[0]} = e^{-k^2 \delta^2 a} \tag{B7}$$

It is readily seen that the amplitude reduction is a function of the degree of smoothing and the wave number. The shorter the wave (large k) or the greater the smoothing (larger a) the more the amplitude will be reduced.

In practice equation (B1) is integrated by repeated applications of the del square operator with varying increments in a $(a_1, a_2, \cdots, a_n)$. It can be seen from equation (B5) that the resultant smoothing is cumulative in a since

$$\begin{aligned} \phi[a_1][a_2] &= \phi[0][a_2]\, e^{-k^2 \delta^2 a_1}, \\ &= \phi[0]\, e^{-k^2 \delta^2 (a_2 + a_1)} = \phi[a_1 + a_2] \end{aligned} \tag{B8}$$

In explicit finite difference form:

$$\phi[a_1] = \phi[0] + \nabla^2 \phi[0]\, a_1$$

$$\phi[a_1 + a_2] = \phi[a_1] + \nabla^2 \phi[a_1]\, a_2$$

$$\vdots$$

$$\phi\left[\sum_{i=1}^{n} a_i\right] = \phi\left[\sum_{i=1}^{n-1} a_i\right] + \nabla^2 \phi\left[\sum_{i-1}^{n-1} a_i\right] a_n \tag{B9}$$

where ∇^2 is the five-point finite difference del operator on a lattice with gridlength δ . In general the a_i are not equal, but for reasons of numerical stability increase with successive steps.

Smoothing is complete when $a = \sum a_i$ reaches a predetermined value. $\phi\,[a]$ is then the long-wave component field, and the short-wavelength component field is formed by subtracting the long-wave from the original field.

The degree of smoothing is assigned by deciding on the reduction factor to be applied to a particular wavelength. In order to elucidate this point, it is convenient to construct the general smoothing curve (filter) from equation (B7) with the wave number replaced by the wavelength in grid increments.

$$K = 2\pi / n\delta \tag{B10}$$

where n is the number of gridlengths corresponding to K. Then

$$R = e^{-4\pi^2 a/n^2} \tag{B11}$$

Using equation (B11) it is possible to plot a series of curves corresponding to different n for the reduction factor as a function of a . However, a single general curve can be constructed by introducing a new variable x which is a function of both a and n:

$$rx^2 = 4\pi^2 a/n^2 \tag{B12}$$

where r is an arbitrary positive constant used to scale x (as will become apparent).

Thus from (B11)

$$R = e^{-rx^2} \tag{B13}$$

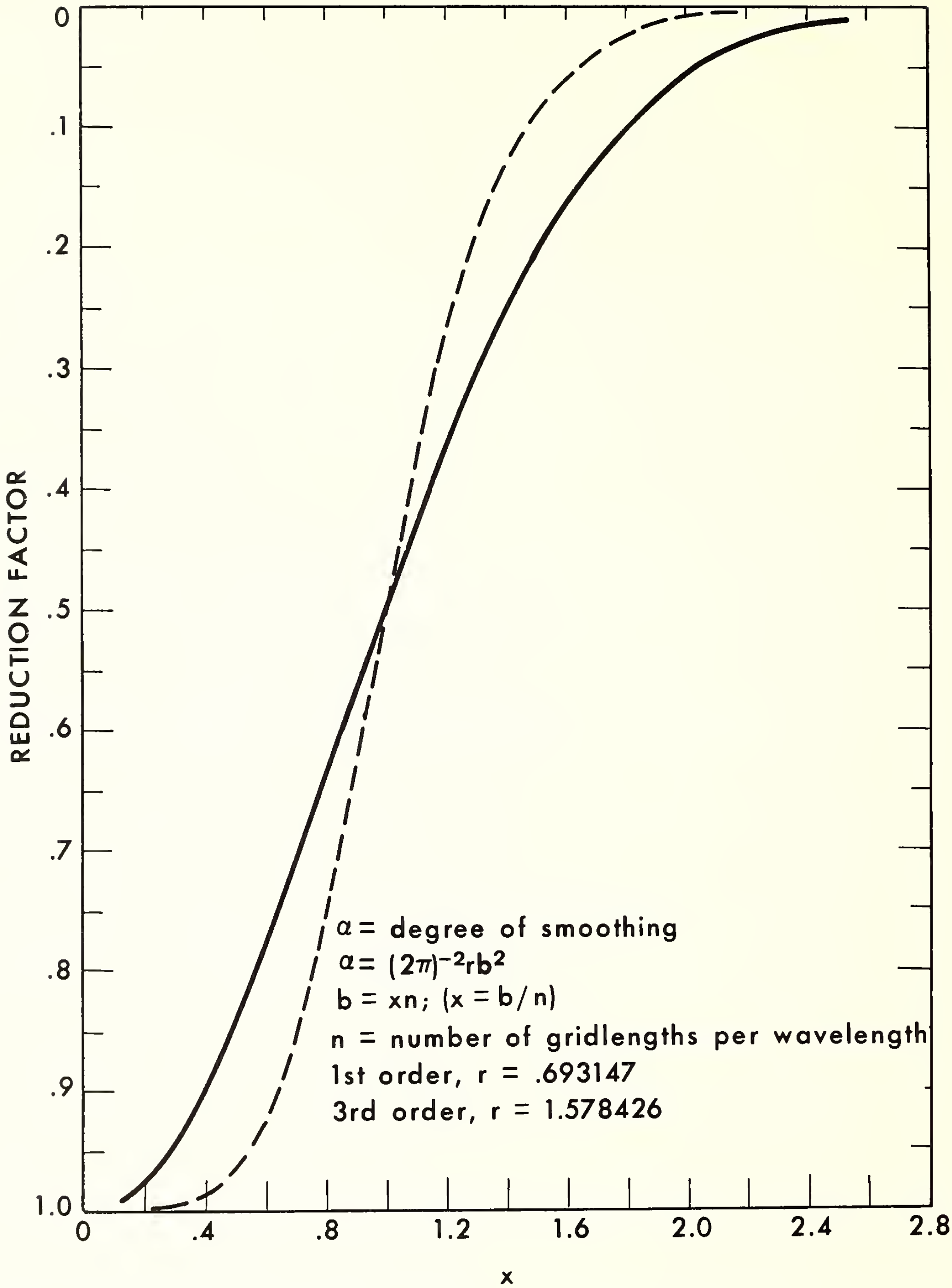

Figure 18.--Normalized filter curves for first- and third-order smoothing.

For plotting purposes it is convenient to define r by requiring that R = .5 when x = 1. Using this definition in equation (B13), r = .693147. The filter curve is depicted by the solid line in figure 18.

To demonstrate the use of the curve, suppose that we decide to apply the smoother until a 10-gridlength wave is reduced to 10 percent of its original amplitude. From figure 18 we find that for R = .1, x = 1.82. Using equation (B12) and the definition of r, we find that the proper degree of smoothing is a = 5.8.

Because n is linearly dependent on x, the slope of the curve in figure 18 depicts the sharpness of the filter. A perfect filter would be a vertical line at x = 1. All shorter wavelengths (smaller n, larger x) would be entirely removed (R = 0), whereas all longer wavelengths would be entirely retained (R = 1). The filter described by the smoothing considered above (hereafter called first-order smoothing) is not particularly sharp. The fact that the filter is not sharp means that the scale separation is imperfect. The long-wavelength field contains some components of the short-wavelength field and vice versa. This undesirable feature can be corrected, at the expense of computation time, by applying higher order filters.

The principle of higher order smoothing is conceptually simple. For example, suppose that the short-wavelength field after first-order smoothing contains 95 percent of the amplitude of a particular short wave and erroneously contains 15 percent of the amplitude of a particular long wave (present because of the imperfection of the filter associated with first-order smoothing). If after completion of first-order smoothing the short-wavelength field is further smoothed into large and small scale components, the amplitude of the long wave will be reduced in the second short-wavelength component field to .15 X .15 or 2.25 percent of its original amplitude. The amplitude of a short wave will be reduced in the second short-wavelength component field to . 25 X .95 or 90.25 percent of its original amplitude. This second-order smoother is certainly sharper than the first-order smoother because the longer wavelengths are filtered more rapidly than the shorter. In fact, as will now be shown analytically, the repeated smoothing of the residual field can be extended to give a filter of any desired sharpness.

Equation (B2) for first-order smoothing can be rearranged to give

$$\phi[0, a] = \phi[0] - \phi[a] \qquad \text{(B14)}$$

Second-order smoothing as described above involves smoothing the residual field a second time:

$$\phi[0\cdot a][0,a] = \left\{\phi[0]-\phi[a]\right\}[0,a]$$

$$= \phi[0][0]-\phi[0][a]-\phi[a][0]+\phi[a][a] \qquad (B15)$$

From equation (B8)

$$\phi[0,a]\lceil 0,a] = \phi[0]-2\phi[a]+\phi[2a] \qquad (B16)$$

Adopting the convention

$$\phi[a][a] = \phi[2a] = \phi[a]^2 \qquad (B17)$$

equation (B16) can be written

$$\phi[0,a]^2 = \phi\left(1-[a]\right)^2$$

(B18)

or in general

$$\phi[0,a]^N = \phi\left(1-[a]\right)^N$$

The final long wave component field after nth degree smoothing is then found by subtracting the residual from the original field:

$$\phi_{LW} = \phi[0]-\phi[0,a]^N = \phi\left\{1-\left(1-[a]\right)^N\right\} \qquad (B19)$$

For reasons of economy we have adopted third-order smoothing. The corresponding long-wavelength field is readily shown to be

$$\phi_{LW} = 3\phi[a] - 3\phi[2a] + \phi[3a] \qquad \text{(B20)}$$

As shown by equation (B20), the long-wavelength field is found in practice not by repeatedly smoothing the residual field but by smoothing the original field to $3a$. This is computationally more efficient because, as mentioned earlier, as smoothing progresses larger smoothing increments can be taken (viz., equation (B9)).

Using equations (B5), (B6), (B7), (B10), and (B12) with (B20), the reduction factor for third-order smoothing is

$$R = 3e^{-rx^2} - 3e^{-2rx^2} + e^{-3rx^2} \qquad \text{(B21)}$$

Again adopting the convention that R = .5 when x = 1, r = 1.5784264. The third-order filter curve is plotted as a dashed line on figure 18. As anticipated, the third-order filter is considerably sharper than the first-order filter.

To use the third-order smoother, suppose as before that we wish to reduce a 10-gridlength wave to 10 percent of its original amplitude. From the figure we find that from R = .1, x = 1.46. Using equation (B12) and the definition of r, we find that the proper degree of smoothing is a = 8.52.

Equation (B1) describes the procedure for explicit smoothing. In practice implicit smoothing is found to be more efficient. One smoothing cycle is represented by

$$\phi[a+da] = \phi[a] + \frac{da}{2}\left\{\nabla^2\phi[a] + \nabla^2\phi[a+da]\right\} \qquad \text{(B22)}$$

The field is solved by standard overrelaxation using a relaxation factor

(Holl, 1967) ω equal to

$$\omega = 1 + \left[\frac{q^2}{1+(1-q^2)^{1/2}} \right] \tag{B23}$$

where

$$q = 2\delta a/(2\delta a + 1) \tag{B24}$$

The δa for each smoothing cycle is assigned such that 15 cycles will give fields smoothed to a , 2 a , and 3 a . A normalized table for δa^* is given in table 7. The actual δa used in each cycle is found by multiplying the normalized value by the desired degree of smoothing.

Table 7.--Normalized smoothing increments (from Holl, 1967)

Cycle No.	δa^*	Σa^*	Cycle No.	δa^*	$\Sigma \delta a^*$
1	.006	.006	9	.154	.448
2	.009	.015	10	.230	.678
3	.014	.029	11	.322	1.000
4	.020	.049	12	.500	1.500
5	.030	.079	13	.500	2.000
6	.045	.124	14	.500	2.500
7	.068	.192	15	.500	3.000
8	.102	.294	--	--	--

APPENDIX C

Program

```
      SUBROUTINE SCALE
      DIMENSION F1(3021),F2(3021),F3(3021),MFAC(3021),ZOUT(3021)
      COMMON F1,F2,F3,MFAC,ZOUT
      REAL MFAC
C     IMPLICITE SCALE SEPARATION PROGRAM DESIGNED BY M.M.HOLL
C     PROGRAMMED BY C.HAYDEN AND R.NAGLE NOAA NESS
C     FIELD TO BE SMOOTHED ENTERS INTO F1(ORIGINAL) AND IS OPERATED ON
C     BY SUBROUTINE SCLN(N,II) FROM F2. ORIGINAL FIELD MUST BE A 53 X57
C     ARRAY AND SCALED IN METERS. NINETY-FIVE(95) PERCENT OF THE
C     AMPLITUDE OF WAVE NUMBER 10 (OR HIGHER) IS ELIMINATED FROM THE
C     ORIGINAL FIELD BY THIS PROGRAM, THE RESULTING FIELD IS CALLED
C     THE LONG WAVE PATTERN (SR). THE SR FIELD IS CONTAINED IN F3.
      THE PORTION OF THE ORIGINAL FIELD WHICH HAS BEEN REDUCED BY THE
C     SMOOTHING PROCESS MAY BE RETRIEVED BY SUBTRACTING THE SR FIELD
C     FROM THE ORIGINAL, THIS (SD) IS FOUND IN F2.
C     THE SMOOTHING IS ACCOMPLISHED BY OVER-RELAXATION. THE ORIGINAL
      FIELD IS SMOOTHED TO ALPHA=1, THEN TO ALPHA=2 AND ALPHA=3.
C     THE SR FIELD IS PRODUCED AS FOLLOWS
C     SR=3*Z(ALPHA=1)-3*Z(ALPHA=2)+Z(ALPHA=3) WHERE Z(ALPHA=1) REPRE
C     SENTS THE ORIGINAL FIELD SMOOTHED TO ALPHA=1 AND SO ON
C     NO INPUT-OUPUT ROUTINES ARE PROVIDED
      CALL MFACTR
      N=5
C     SMOOTH TO ALPHA1=5 AND STORE RESULTING FIELD IN ZOUT
      DO 10 I=1,11
      CALL SCLN(N,I)
   10 CONTINUE
      DO 20 I=1,3021
      ZOUT(I)=F2(I)
   20 CONTINUE
C     SMOOTH TO ALPHA2=10, COMBINE WITH 3*Z(ALPHA=1)AND STORE IN ZOUT
      CALL SCLN(N,12)
      CALL SCLN(N,13)
      DO 30 I=1,3021
      ZOUT(I)=3.*(ZOUT(I)-F2(I)
   30 CONTINUE
C     SMOOTH TO ALPHA3=15
      CALL SCLN(N,14)
      CALL SCLN(N,15)
C     FORM SR AND SD FIELDS
      DO 40 I=1,3021
      F3(I)=ZOUT(I)+F2(I)
      F2(I)=F1(I)-F3(I)
   10 CONTINUE
      RETURN
      END
```

```
      SUBROUTINE MFACTR
      DIMENSION F1(3021),F2(3021),F3(3021),MFAC(3021),FLAT(3021),
     1ZOUT(3021)
      COMMON F1,F2,F3,MFAC,ZOUT,FLAT
      REAL MFAC
      PIB2=3.1415926/2.
      RCON=31.20435919
      CKCON=5.*3.1415926/180.
      DO 10 J=1,57
      L=(J-1)*53
      DO 10 I=1,53
      K=L+I
      FJ=J-29
      FI=I-27
      R=SQRT(FI*FI+FJ*FJ)
      FLAT(K)=PIB2-2.*ATAN(R/RCON)
      IF(FLAT(K).LT.CKCON)5,6
    5 SL=SIN(CKCON)
      GO TO 7
    6 SL=SIN(FLAT(K))
    7 S=1.86602/(1.+SL)
      FLAT(K)=SL
   10 MFAC(K)=S*S
   25 CONTINUE
      RETURN
      END
```

```
      SUBROUTINE SCLN(N,II)
      DIMENSION F1(3021),F2(3021),F3(3021),MFAC(3021),B(3021),DA(15)
      COMMON F1,F2,F3,MFAC
      EQUIVALENCE (F3,B)
      REAL MFAC
      DATA (DA=.006,.009,.014,.02.,03,.045,.068,.102,.154,.230,.322,.5,
      1.5,.5,.5)
      DAL=DA(II)*N
      DO 10 J = 2,56
      L = (J-1)*.53
      DO 10 I = 2,52
      M = L + I
      B(M) = F2(M)+DAL*MFAC(M)*(F2(M+1)+F2(M-1)+F2(M+53)+F2(M-53)
     1-B*F2(M))/2
   10 CONTINUE
      QB=2.*DAL/(2.*DAL+1.)
      DAL = DAL/2.
      QBS = QB*QB
      OM = QBS/(1.+SQRTF(1.-QBS))
      OMEGA = 1.+OM*OM
      KK = 0.
   12 KK=KK+1
      IF(KK.GT.10)GO TO 30
      ICON = 0
      DO 15 J = 2,56
      L = (J-1) * 53
      DO 15 I = 2,52
      M = L + I
      R = (DAL*MFAC(M)*(F2(M+1)+F2(M-1)+F2(M+53)+M-53)) + B(M))/(1.+4.
     1*DAL*MFAC(M))-F2(M)
      RR = R*R
      IF(RR.GT.25.)ICON = ICON+1.
      F2(M) = F2(M) +OMEGA*R
   15 CONTINUE
      IF (ICON.GT.0)GO TO 12
   20 RETURN
   30 PRINT 40
   40 FORMAT(* SCALE NOT CONVERGING*)
      STOP
      END
```

☆ U. S. GOVERNMENT PRINTING OFFICE : 1971 O - 420-778